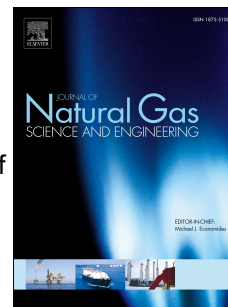


Journal Pre-proof

CO emissions and temperature analysis from an experimental and numerical study of partially premixed methane flames impinging onto a cooking pot

Saúl Laguillo, José Salvador Ochoa, Eduardo Tizné, Antonio Pina, Javier Ballester, Alfredo Ortiz



PII: S1875-5100(20)30625-9

DOI: <https://doi.org/10.1016/j.jngse.2020.103771>

Reference: JNGSE 103771

To appear in: *Journal of Natural Gas Science and Engineering*

Received Date: 12 August 2020

Revised Date: 19 November 2020

Accepted Date: 19 December 2020

Please cite this article as: Laguillo, S., Ochoa, J.S., Tizné, E., Pina, A., Ballester, J., Ortiz, A., CO emissions and temperature analysis from an experimental and numerical study of partially premixed methane flames impinging onto a cooking pot, *Journal of Natural Gas Science & Engineering*, <https://doi.org/10.1016/j.jngse.2020.103771>.

This is a PDF file of an article that has undergone enhancements after acceptance, such as the addition of a cover page and metadata, and formatting for readability, but it is not yet the definitive version of record. This version will undergo additional copyediting, typesetting and review before it is published in its final form, but we are providing this version to give early visibility of the article. Please note that, during the production process, errors may be discovered which could affect the content, and all legal disclaimers that apply to the journal pertain.

© 2020 Elsevier B.V. All rights reserved.

© 2020. This manuscript version is made available under the CC-BY-NC-ND 4.0 license <http://creativecommons.org/licenses/by-nc-nd/4.0/>

CRediT author statement

Saúl Laguillo: Conceptualization, Methodology, Software, Validation, Formal analysis, Investigation, Resources, Data Curation, Writing - Original Draft, Writing - Review & Editing, Visualization.

José Salvador Ochoa: Conceptualization, Methodology, Software, Validation, Formal analysis, Investigation, Resources, Writing - Original Draft, Writing - Review & Editing, Visualization, Supervision, Project administration.

Eduardo Tizné: Methodology, Validation, Investigation, Resources.

Antonio Pina: Methodology, Validation, Investigation, Resources.

Javier Ballester: Conceptualization, Methodology, Validation, Formal analysis, Supervision.

Alfredo Ortiz: Conceptualization, Methodology, Validation, Formal analysis, Writing - Review & Editing, Project Administration.

CO emissions and temperature analysis from an experimental and numerical study of partially premixed methane flames impinging onto a cooking pot

Saúl Laguillo^a, José Salvador Ochoa^b, Eduardo Tizné^c, Antonio Pina^c, Javier Ballester^c, Alfredo Ortiz^{a,*}

^a *Department of Chemical and Biomolecular Engineering. University of Cantabria, Av. Los Castros 44, 39005, Santander, Cantabria, Spain.*

^b *Gas Competence Center, Product Division Cooking, BSH Home Appliances Group, Avda. Eduardo García del Río 30, 39011, Santander, Cantabria, Spain.*

^c *Laboratory for Research on Fluid Dynamics and Combustion Technologies (LIFTEC), Univ. Zaragoza/CSIC. C/ María de Luna 3, 50018, Zaragoza, Spain.*

Abstract

The increase of thermal efficiency compatible with low carbon monoxide (CO) emissions is a challenging and permanent target in the design of any burning technology such as domestic gas cooking burners. The main goal of this work is to provide a deeper insight into the CO formation and its relationship with the flame structure when natural gas (NG) is burnt in these devices. Given their geometrical complexity, a simpler configuration is employed to carry out new experimental tests assuming similar operating conditions. Then, numerical modeling is validated and subsequently used to deeply analyze the flame-wall interaction phenomena. The simplified burner consists of an axisymmetric, partially premixed methane flame impinging perpendicularly onto the bottom wall of a water pot. The influence of burner-to-pot distance, flame thermal power, primary aeration and inside-pot water temperature on CO emissions and thermal efficiency is evaluated. A decrease in CO emissions is observed as primary aeration or wall temperature increases. Nevertheless, non-monotonic trends appear for changes in burner-to-pot distance or flame thermal power. The trends are numerically well captured selecting the detailed GRI-Mech 3.0 chemistry mechanism. The analysis of the computational results reveals that CO emissions and thermal efficiency are strongly related to the relative boundary position of the inner premixed flame cone and the wall. The growth of the distinct zones of the flame where CO chemically reacts with primary and secondary air is constrained by the presence of the pot wall. This fact drives the final CO concentration, and incidentally the thermal efficiency, leading to a factual criterion for the design of NG burners.

Keywords: Methane, flame-wall interaction, carbon monoxide, single flame burner, partially premixed flame, inner premixed flame cone.

*Corresponding author

Email address: ortizal@unican.es (Alfredo Ortiz)

⁰ Abbreviations: NG: Natural Gas; FWI: Flame-Wall Interaction; CFD: Computational Fluid Dynamics; LIF: Laser Induced Fluorescence; LPG: Liquefied Petroleum Gas; SW: Side Wall; PID: Proportional, Integral, Derivative; PTFE: PolyTetraFluoroEthylene; BC: Baseline Case; SST: Shear Stress Transport; DOM: Discrete-Ordinate Model; PRESTO: PRessure STagging Option; HTC: Heat Transfer Coefficient; COAF: CO Air Free; NDIR: Non-Dispersive InfraRed.

1. Introduction

Carbon monoxide (CO) is considered a poisoning pollutant due to the harmful effects on human health when exposed to prolonged inhalation of moderate concentrations of this gas. These effects could include occasional episodes of headaches, fatigue, and dizziness, till chronic heart diseases depending on the exposure period [1]. In indoor environments, CO is largely produced by combustion sources such as cooking and heating appliances producing smoke. Although appropriate venting installations can avoid unhealthy concentrations of pollutants, practically all the countries and manufacturers limit the production of CO from combustion devices by standards specifying threshold values [2]. In a domestic gas cooking burner, the combustion process is altered due to the interaction between flame and solid elements such as thermocouples, grills or pots. This phenomenon, so-called flame-wall interaction (FWI), induces perturbations and quenching of chemical reactions which may lead to undesirable effects in pollutant emissions and heat exchange [3, 4, 5, 6]. For hydrocarbon fuels such as natural gas (NG), a CO threshold value and the requirement of high efficiency to minimize the CO₂ emissions [7] constrains the possibilities in the design of this type of configurations.

The accurate prediction of this species is one of the greatest challenges facing numerical simulations and therefore during the design process of gas cooking burners. The combination between their complex geometries and the need to precisely describe chemical kinetics (skeletal or detailed chemistry) results in a huge computational load, which makes this type of analyses practically unaffordable. The detailed experimental characterization of realistic, multiple-flame cooking burners is also a challenging task, mainly due to their highly three-dimensional nature [8, 9, 10] and the variety of their designs [11, 12]. Therefore, simpler configurations are commonly used to analyze the chemistry and the FWI phenomena that take place during the combustion process. For this purpose, geometrically simpler burners with a single flame (Bunsen-like burner) perpendicularly impinging onto a wall have been frequently employed. This type of configurations can reproduce most of the relevant features and work in representative conditions of those present in domestic gas cooking burners. Furthermore, they afford a detailed definition of operating variables and boundary conditions, which is crucial to subsequently analyze the process through computational fluid dynamics (CFD) simulations.

In general, domestic gas cooking burners operate at partially premixed conditions [13]. Hence, the flame presents two distinct regions. A fraction of the fuel burns in a thin laminar premixed flame. For an axisymmetric configuration, this flame is approximately conical, with a cold core of unreacted fuel-air mixture [14]. In practical NG cooking burners, the primary aeration (defined as the reciprocal of equivalence ratio) is usually in the range 0.4-0.7 [8, 15, 16], so that a large fraction of unreacted fuel remains downstream of the premixed flame. This leads to the formation of a second combustion stage, where the remaining fuel is gradually mixed with the surrounding air and burns in a diffusion flame. Understanding this structure and how these two different zones of the flame interact with a solid wall is relevant for the global burning rate and the pollutant formation [17].

A great number of studies regarding the interaction between a single methane flame and a wall have

been published. Most of them are focused on the experimental analysis of heat transfer and the influence of parameters such as burner internal geometry [18, 19], burner diameter [20, 21, 22], thermal power [23], equivalence ratio [24, 25], and burner-to-plate spacing [26, 27, 28]. The effect of these parameters on flame stability was studied by Hsieh and Lin [29], while Hou and Ko [30] and Kuntikana and Prabhu [31] analyzed their combined effect with oblique angle on flame structure, temperature distribution and thermal efficiency. Moreover, Tajik et al. [32] included heat flux distribution under the effect of varying inlet gas temperature. Some of these works are supplemented with CFD simulations to explain the distribution of the heat flux [21, 22, 23, 27, 32]. All the aforementioned studies show that those parameters have a significant influence on heat transfer rate and surely determine the final efficiency of the process. However, only a few investigations include the analysis of pollutant emissions in this type of configurations. Saha et al. [33] carried out some experiments with impinging rich methane and ethylene jet flames, analyzing the effect of Re number, equivalence ratio, and burner-to-plate separation distance on heat transfer and emissions. CO and NO_x concentrations were measured in the flue gas leaving the wall surface. The results show that the CO emission increases when burner-to-plate spacing is lowered, or Re number is increased, since in both situations the combustion do not reach completion within the wall jet region. Other studies [34, 35] carried out CO measurements with laser induced fluorescence (LIF) for variations in impinging methane/air flames at lean, stoichiometric, and rich conditions, comparing their findings to numerical predictions. Chien et al. [36] also utilized LIF to correlate CO emission with variations in the structure of nonpremixed methane/air flames and OH distribution, as a function of burner-to-plate distance. Li et al. [37, 38] and Mishra [39] included CO/NO_x emissions analyses in their studies of a premixed flame jet impinging on a flat wall, varying plate temperature, Re number, equivalence ratio, and nozzle to plate distance, but using liquefied petroleum gases (LPG) as fuel instead of methane.

In all the previous studies, pollutant measurements are performed in the vicinity of the flame, and local single-point data are reported. However, although relevant, these values may greatly differ from those downstream of the impingement zone, which are more interesting to draw conclusions for practical domestic gas burner configurations. According to the European Standard certification [2], the emissions' sample must be captured in the upper part of a hood, in the exhaust gas stream where there is no combustion process and species concentrations have reached a stable value. The present work addresses this issue through a similar configuration as the one used in certification tests of gas cooking burners.

Hence, the main goal of this study is to provide a deeper insight into the CO formation and its interrelationship with relevant performance parameters in a FWI configuration during the NG combustion. To do so, new experimental data are obtained and on-purpose validated CFD simulations are carried out under similar physical conditions of domestic gas cooking burners. The workbench, specifically designed and constructed for this study, consists of a single, partially premixed flame, impinging perpendicularly onto the bottom of a pot filled with cooled water. Pure methane is fed as fuel, given that it is the main component and the usual reference gas for NG combustion [40, 41]. Temperature

and CO emissions are evaluated under certain ranges of burner-to-pot distance, thermal power, inside-pot water temperature, and degree of premixing. These ranges encompass the values present in real gas cooking burners using NG as fuel. Outcomes from the experiments include: temperature values of the internal and external pot walls, inside-pot water temperature, jet velocity field (non-reacting flow), spatial distribution of the flame temperature, and CO and CO₂ emission concentration in the exhaust gases at the top of the hood (as it is done in the certification tests). Once the experimental program is completed and used to validate the computational model, the analysis is mainly based on the numerical results to obtain a complete description of the phenomena. The evaluation of additional intermediate operating conditions paves the way for a more precise tracking of the boundary of the inner premixed flame cone, elucidating its interaction with the wall. A novel approach based on the inclusion of a transport equation for a passive scalar facilitates the distinction of two CO-involving reaction regions: (1) primary-air premixed zone, and (2) secondary-air diffusion zone. The specific interaction of these zones with the wall distinctively alters their growing, driving to the final CO concentration, and bounding incidentally the thermal efficiency. This fact can lead to a factual criterion for the design of NG cooking burners.

2. Experimental setup and procedure

2.1. Workbench description

The experimental facility used in this work was designed to study partially premixed flames impinging on a cold wall under closely controlled conditions. A general view is shown in Figure 1 and the main elements are described hereinafter.

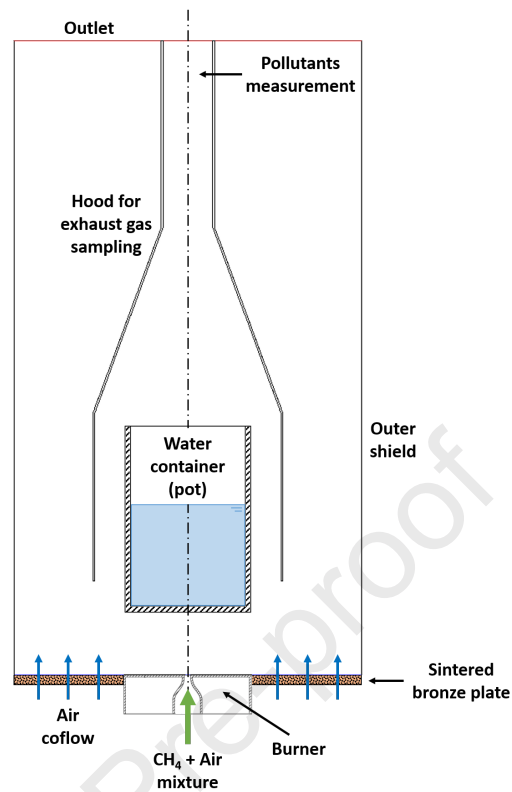


Figure 1: Schematic representation and main elements of the single flame burner experimental setup.

2.1.1. The burner

The air-fuel mixture is injected through a convergent nozzle ending in a circular orifice of 5 mm in diameter. The nozzle inner shape was designed to produce a very flat velocity profile at the exit and minimize turbulence intensity. Injector walls are surrounded by a cavity (100 mm in diameter) within which cold water is recirculated to maintain a constant and low temperature (around 300 K), recorded by means of two wall thermocouples welded on the injector and the front wall respectively. These measurements are essential in order to know inlet gas and burner wall temperatures. A premixer is included upstream to ensure homogeneity of the air-fuel mixture.

2.1.2. Outer shield and air co-flow

To avoid flame perturbations due to laboratory air movements, the whole setup is protected by a cylindrical shield (280 mm diameter). Besides, a coaxial air flow is forced through a sintered bronze disk installed around the burner piece. The high pressure drop across the sintered element guarantees a flat velocity profile, which value is adjusted at 0.05 m/s in all the tests. The combination of the outer shield and the co-flow provides a controlled and known ambient around the burner, as required to specify boundary conditions for the numerical simulations.

2.1.3. The water pot

The flame impinges on the bottom of a perfectly cylindrical water container, made in stainless steel, with a height of 150 mm, and 93 and 101 mm of inner and outer diameter respectively. Since the pot imposes a critical thermal boundary condition, the bottom is carefully instrumented to determine temperature and heat flux radial profiles (see Figure 2). Ten thermocouples are inserted into the 5 mm thickness bottom wall, identified as S0-S4 (water, upper side) and F0-F4 (flame, bottom side). They are distributed at the same radial distances in order to obtain temperature profiles, local axial temperature gradient and, hence, local heat flux. Additional thermocouples are inserted into the side wall (SW) and in the water (W).

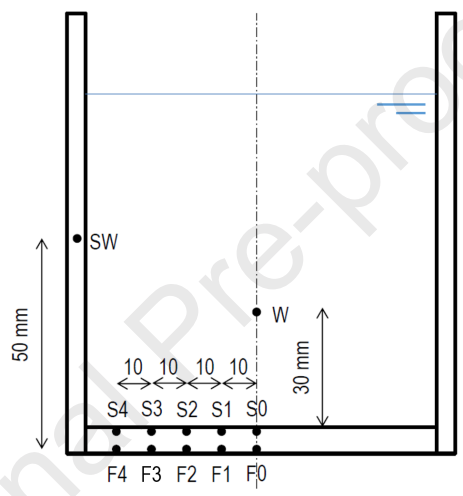


Figure 2: Scheme of the water pot with the location of the thermocouples embedded in the bottom wall (F* and S*), the side wall (SW), and inside the water (W).

The pot is closed with a lid, which is designed in such a way that the water condensed on its bottom side drops again into the pot, so that the vapor losses are very low and the level remains virtually constant during the experiments. Water temperature is also maintained constant throughout each test duration, so that data are collected for perfectly stable conditions. This is achieved by forcing the circulation of water through an outer loop with a diaphragm pump. Depending on the desired temperature, the loop can include a coil immersed in a cold water bath. By adjusting the length of the outer loop and optionally passing the water through the coil, water temperature can be held sensibly constant at different set points. In particular, tests are performed at 308 K, 323 K, and 338 K. The water pot is supported on three rods welded on the top of the pot so as not to disturb the gas flow. This supporting system can be adjusted laterally as well as in height, in order to get the pot perfectly centered with respect to the injector and outer shield, and regulating the burner-to-pot distance as required for the various tests.

2.1.4. The hood

Combustion products generated in the flame and flowing around the pot are collected in the upper part by a hood. It discharges through a cylindrical duct, where the gas sampling probe is installed. This probe consists of a stainless steel duct with several side orifices at selected points, to further ensure that the gas sample is representative of the average gas composition.

2.1.5. Support structure

All the aforementioned components are assembled and supported on a mounting structure that includes all the necessary elements to hold them and finely adjust their relative position, as required for the conditions of the different tests.

2.2. Instrumentation and measurement techniques

The set of data collected in the tests is obtained with different instruments and techniques:

- Local gas velocity (under cold-flow conditions) is measured with constant-temperature hot wire anemometry (TSI, model IFA 300). Two-wire sensors are used to simultaneously obtain axial and radial velocity components, as well as their cross-correlation. These measurements typically present an uncertainty of $\pm 1\%$ [42].
- Local gas temperatures are measured with a bare fine wire, S-type (Pt-Pt10%Rh) thermocouple, which is mounted on a 3-D traversing system to register between 1000 and 2000 mean temperature values across the flame, depending on the case. The sensing element consists of butt-welded 70 μm wires, supported on thicker (350 μm) wires of the same material. These are inserted into a two-bore alumina rod, which provides the required rigidity for accurate positioning in the flame. In-flame temperature measurements can be affected by conduction and radiation errors. The fine thermocouples used in this work have a length/diameter ratio >150 , enough to make the conduction error negligible. As for the radiation error, the measurements are corrected by:

$$T_{gas} = T_{TC} + \frac{D_{wire} * \epsilon * \sigma * (T_{TC}^4 - T_{wall}^4)}{\kappa_{gas} * (0.35 + 0.65 * Re_{wire}^{0.45})}, \quad (1)$$

where T_{gas} is the real temperature of the gas, T_{TC} is the temperature measured by the thermocouple, and T_{wall} is the temperature of the surrounding cold walls (all of them in K); D_{wire} is the wire diameter (m); ϵ is the emissivity of the thermocouple; σ is the Stefan-Boltzmann constant ($\text{W}/\text{m}^2 * \text{K}^4$); κ_{gas} is the thermal conductivity of the gas ($\text{W}/\text{m} * \text{K}$); and Re_{wire} is the Reynolds number calculated from the wire diameter and the density, viscosity, and velocity of the gas [43, 44]. Overall, the uncertainties due to the thermocouple material and the radiation correction are estimated to be around 10 K.

- Water, burner and pot wall temperatures are measured by stainless steel sheathed K-type thermocouples, which typically have an uncertainty of ± 2.2 K or $\pm 0.75\%$.

- Fuel, primary combustion air and secondary co-flow air mass flow rates are controlled and automatically regulated by three mass flow meters of the thermal type, supplied by the Bronkhorst company. They are connected in closed-loop to a control valve through PID (proportional, integral, derivative) regulators in order to ensure good accuracy and avoid oscillations or drifts during the tests. Since the flow rates are above 20% of the measurement range in all the tests, the accuracy is always better than 1%, as defined by the supplier. This also applies to any derived parameter, like power, velocity at the injector outlet, or primary aeration.
- The gas sample collected at the hood outlet is sent by means of PTFE (Polytetrafluoroethylene) tubing to a set of individual on-line gas analyzers (non-dispersive infrared (NDIR), manufactured by Emerson), where O₂, CO₂, and CO concentrations are measured on a dry basis. Associated uncertainty in the results of CO is mainly due to the reproducibility of the whole test and measurement process.
- A computer-controlled three-dimensional traversing system is employed to obtain the two-dimensional maps of temperature and velocity at different axial and radial coordinates. After programming the measurement grid and setting the origin of coordinates with respect to a reference point, this device automatically displaces the tip of the sensor to the selected points with very good accuracy (± 0.02 mm).
- A color video camera is placed next to the flame zone in order to record direct imaging of the flames.

In all the cases, the test is performed in duplicate, with an associated maximum standard deviation of 2 K in registered wall temperatures and 5% in carbon monoxide measurements.

2.3. Operating conditions

Discrete values of the studied parameters are chosen to cover operating ranges that produce similar flow features to those present in real gas cooking burners. Flame thermal power (\dot{P}) is varied from 250 to 500 W, corresponding to Re numbers roughly between 700 and 1400. These \dot{P} values are selected in order to obtain a velocity magnitude value at the injector outlet similar to the ones present at the ports of a domestic gas cooking burner, typically between 2 and 5 m/s, and specified by fixing the mass flow rate at the inlet. Primary aeration, defined by the air-fuel equivalence ratio (lambda, λ), relates local and stoichiometric mixture conditions, and can be calculated by

$$\lambda = 1/\Phi = \frac{(Y_{air}/Y_{fuel})}{(Y_{air}/Y_{fuel})_{stoich.}}, \quad (2)$$

where Φ is the fuel-air equivalence ratio and Y stands for the mass fraction of the mixture components. λ ranges between 0.35 to 0.65. Burner-to-pot distance, fixed at 20, 50 and 80 mm, is represented by the H/d ratio (4, 10 and 16), where H is the distance between the injector and the pot bottom wall, and d is the injector inner diameter. Finally, inside-pot water temperature (T_{water}) is modified between 308

and 338 K. Conditions for the baseline case (BC) are: $\dot{P}=375$ W, $\lambda=0.5$, $H/d=10$, and $T_{water}=323$ K. The test program for reacting cases is designed to perform parametric studies about this central case and includes a total of 15 different test conditions, shown in Table 1. In all these cases the objective is to characterize the main global parameters such as thermal conditions at the pot wall and CO emissions (denoted with **X**). In some selected tests, a detailed temperature field characterization is also performed (**O**).

Table 1: Experimental matrix with test conditions.

\dot{P} [W]	H/d	Water Temperature [K]				
		308	323		338	
		Primary aeration (λ)				
		0.5	0.35	0.5	0.65	0.5
250	4			X		
	10		X	XO	X	
	16			X		
375	4			XO		
	10	X	XO	XO	XO	X
	16			XO		
500	4			X		
	10			XO		
	16			X		

X - Pot temperatures and emissions

O - Temperature field

The flow field is also explored in non-reacting conditions. The characterization of the isothermal jet captures the essential features of the flow (jet development, velocity decay rate, stagnation near the pot wall). For this exploration, the velocity field is measured when injecting only air through the nozzle, with $H/d=10$ burner-to-pot distance and a mean velocity magnitude of 7 m/s at the injector outlet. This value is higher than the fuel injection speed in the reacting cases and also in gas cooking burner ports (2-5 m/s), but was deemed adequate for the purpose of this analysis in order to avoid the increased uncertainties with hot wire anemometry for low velocities [42].

3. Computational setup and procedure

In parallel with the experimental study, CFD simulations are carried out to numerically describe all the phenomena occurring in the system. For this purpose, continuity, momentum, energy, and chemical

species transport equations are solved in a steady-state regime using the software ANSYS Fluent [45].

3.1. Computational domain and mesh

First, the domain and the mesh employed in the computational calculations is described. Given the cylindrical geometry of the setup, a two-dimensional, axisymmetric domain is adopted. The nozzle and the burner inner volumes are not included in the domain, setting directly the boundary condition values at the fuel inlet (injector outlet), burner wall, and air co-flow inlet.

Based on previous experience with this type of configurations, the domain is discretized into ≈ 119 thousand cells for the baseline case ($H/d=10$), with finer resolution in the flame zone, specially in the vicinity of the injector outlet (where chemical reaction starts) and a gradual inflation zone to accurately capture the boundary layer at the hot gas / solid bottom pot wall (see Figure 3).

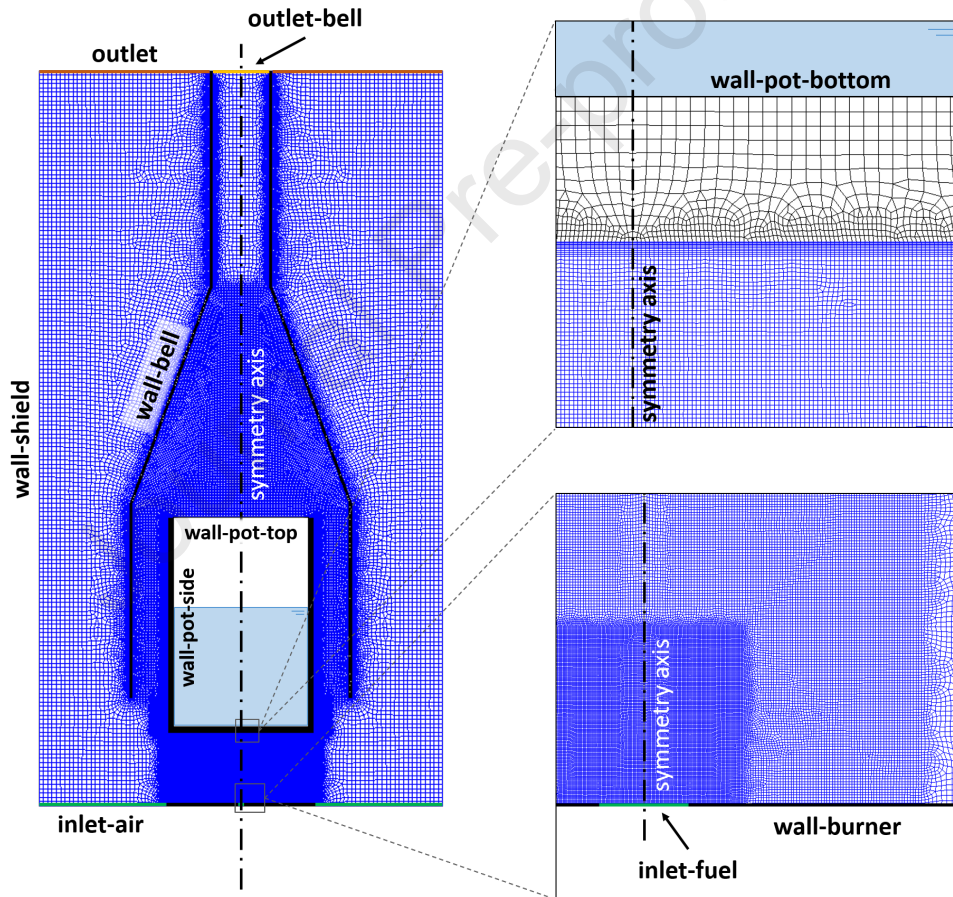


Figure 3: Two-dimensional axisymmetric mesh of the setup with identification of the main zones and boundaries of the computational domain.

In the meshing process, the influence of the mesh resolution on the results is checked. Different simulations are performed, using the same settings and convergence criteria, as shown in Table 2 for the $H/d=10$ case. Four critical variables are monitored: the averaged temperature of the solid pot, and the temperature, CO_2 and CO mole fraction in the exhaust gases stream at the top of the hood. The

agreement between the results obtained with the base and the refined mesh shows the suitability of the original mesh resolution. Same criteria for the rest of the burner-to-pot distance $H/d=4$ and $H/d=16$ cases are followed, resulting in 84 and 154 thousand cells respectively.

Table 2: Results of the refinement study of the mesh for the $H/d=10$ case.

Mesh	Coarser	Base	Finer
Cell number	29713	118852	475408
Cell size (near pot wall resolution, mm)	0.062	0.031	0.016
CPU time (16 cores, s/iteration)	0.76	2.60	8.06
Averaged pot temperature (K)	328.65	328.48	328.48
Temperature (outlet-bell, K)	336.47	332.36	332.48
CO ₂ mole fraction (outlet-bell, %)	1.176	1.205	1.210
CO mole fraction (outlet-bell, ppm)	48.01	156.99	157.65

3.2. Numerical models

This section introduces the main numerical models used in the calculations with ANSYS Fluent.

Regarding the fluid flow model, the experimental configuration was intentionally designed to feed a laminar jet through the injector (Re between 700 and 1400). However, tests revealed that in most of the cases, starting from a very low turbulence intensity, the amplitude of velocity fluctuations starts to grow in the jet after a few millimeters. A transition turbulence model (four-equation Transition SST (shear stress transport) k-omega [46, 47]) is therefore selected to properly capture the decay rate in jet velocity. Despite using this turbulence closure, the combustion is Arrhenius-rate governed (Laminar Finite Rate) by Direct Integration of the chemical kinetics in the Stiff Chemistry Solver of the code, and none turbulence-chemistry interaction is considered.

Net production rate of each chemical species is calculated by adding the specification of gas-phase reactions, thermodynamic and transport properties data contained in special formatted files (Chemkin format). In order to obtain the most reliable results for the chemical species description, the detailed chemistry for methane combustion is considered by employing the GRI-Mech 3.0 mechanism [48].

The mixture is considered to be a multicomponent ideal gas where density depends only on temperature and composition. Kinetic theory is invoked for transport properties such as viscosity, thermal conductivity and mass diffusivity. Radiation is considered by means of the coupled Discrete-Ordinate Model (DOM) [49]. For the Species Model option, the effect of enthalpy transport due to species diffusion in the energy equation (Diffusion Energy Source) is explicitly considered whereas multicomponent diffusion is enabled. Coupled Algorithm for pressure-velocity coupling with PRESTO! (PREssure STaggering Option) scheme for pressure interpolation is selected, whereas second order upwind spatial discretization is applied to the rest of transport variables. A complete overview of the governing equations and their properties can be found in the User's and Theory Guide of the software [45] or

in the Supplementary Material attached to this manuscript.

3.3. Boundary conditions

Specific boundary conditions for the model are summed up in Table 3. The temperatures measured at the injector outlet and burner wall are very stable throughout the experimental tests, in the range 300 ± 1 K. Therefore, a constant value of 300 K is set for the injected fuel and the burner wall temperatures. The radial velocity profile at the injector outlet is imposed as boundary condition for the fuel jet, together with the corresponding air and fuel concentrations in each case ($\lambda=0.35, 0.5$ or 0.65). Water inside the pot is not explicitly included in the computational domain. Instead, the interpolated temperature profile from measurements (S0-S4) is allocated in the pot water-side bottom wall. At the pot side wall, the temperature value is obtained from the thermocouple inserted in that location (SW), and matches with water temperature (308, 323 or 338 K). For internal wall zones in contact with air, convective heat transfer boundary conditions are applied. The burner, the bell, and the pot are constructed of stainless steel, so a value for internal emissivity of $\epsilon=0.4$ [50] is considered.

Table 3: Specific boundary conditions set in the numerical simulation of the flame.

Zone	Type	Thermal condition	Other
inlet-fuel	velocity-inlet	Inlet $T = 300$ K	Exp. velocity profile $\lambda = 0.35/0.5/0.65$
inlet-air	velocity-inlet	Inlet $T = 300$ K	$v_{inlet} = 0.05$ m/s
wall-burner	wall	Fixed $T = 300$ K	
wall-shield	wall	Adiabatic	
wall-pot-bottom	wall	Exp. radial temperature profile	
wall-pot-side (water)	wall	Fixed $T = 308/323/338$ K	
wall-pot-side (air)	wall	Convection (air)	HTC ^a = 15 W/m ² K $T_{\infty} = 308/323/338$ K
wall-pot-top	wall	Convection (air)	HTC ^a = 15 W/m ² K $T_{\infty} = 308/323/338$ K
wall-bell	wall	Conjugate heat transfer	
outlet / outlet-bell	pressure-outlet	Backflow $T = 300$ K	$P_{gauge} = 0$ Pa

^a Heat transfer coefficient

4. Results and discussion

4.1. Non-reacting flow characterization

Previous to simulate the reacting cases, the jet is characterized under cold-flow conditions. For this purpose, the velocity magnitude profile measured along the centerline is compared to those obtained when simulating the non-reacting case enabling the different viscosity models: laminar, turbulence two-equation k-epsilon, turbulence three-equation transition k-kl-omega, and turbulence four-equation transition SST k-omega. Figure 4 shows that the laminar approach is completely inaccurate for these conditions.

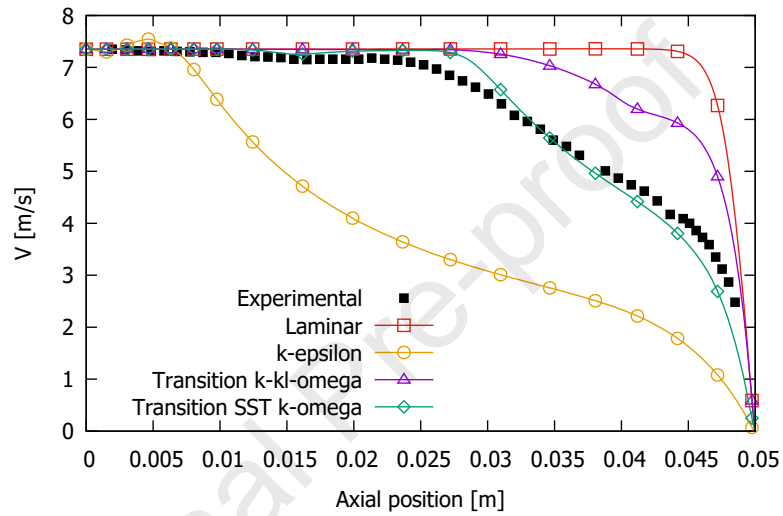


Figure 4: Comparison between experimental and computationally obtained velocity magnitude profiles along the centerline in the non-reacting case.

Among the turbulence models, transition SST k-omega clearly shows the best agreement, with a slight deviation at the beginning of the decay zone (axial position ≈ 0.027 m). The good coincidence between numerical and experimental results is further confirmed by the two-dimensional maps shown in Figure 5a (experimental values are graphically interpolated). In addition, Figure 5b compares normalized contours of root-mean-square velocity (V_{rms}), which is representative of the turbulent fluctuations of the velocity magnitude [51]. It can be observed that turbulence starts to grow only a few millimeters downstream the injector. The transition SST k-omega turbulence model includes a free-stream correlation to relaminarize the flow when turbulent fluctuations are negligible, so it also shows to be valid in the cases when the mean velocity magnitude, and thus the Reynolds number, are lower [46, 47]. Therefore, it is selected to calculate the flow field in all the reacting flow calculations.

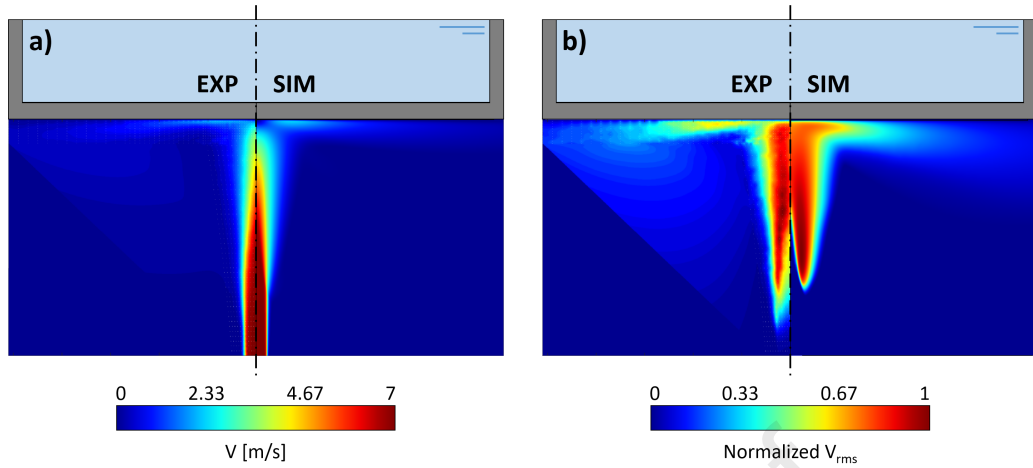


Figure 5: Experimental and transition SST k-omega computational comparison of velocity module (a) and normalized root-mean-square velocity (b) fields.

4.2. Reacting flow characterization

The jet velocity magnitude in the reacting cases is slightly lower (2-5 m/s, depending on the \dot{P}) than the one observed in the non-reacting case (≈ 7 m/s). Despite the lack of experimental measurements of velocity components for the combustion cases, Figure 6a shows the axial velocity decay rate inside the flame for the constant baseline case conditions ($H/d=10$, $\lambda=0.5$, $T_{water}=323$ K) and the three analyzed \dot{P} cases. It can be observed that there is no difference between the laminar and the turbulence model predictions for the lower $\dot{P}=250$ W case. This fact confirms the capabilities of the transition SST k-omega turbulence model to relaminarize the flow when there are no relevant turbulent fluctuations. However, slight differences can be observed for the medium and higher \dot{P} cases. The analysis of the radial pot temperatures shown in Figure 6b determines that the predictions using the SST k-omega turbulence model agree better with measurements and therefore corroborates a more accurate flow field and conjugated heat transfer prediction for the flame-wall interface, mainly in the flame impingement zone. In the rest of the flame field, the differences between laminar and turbulent predictions are negligible as shown in Figure 6c, where the temperature radial profiles near the pot wall (3mm below) show a very good agreement between both numerical predictions and measurements. This fact brings out the suitability of the finite rate chemistry approach without needing a turbulence-chemistry interaction model.

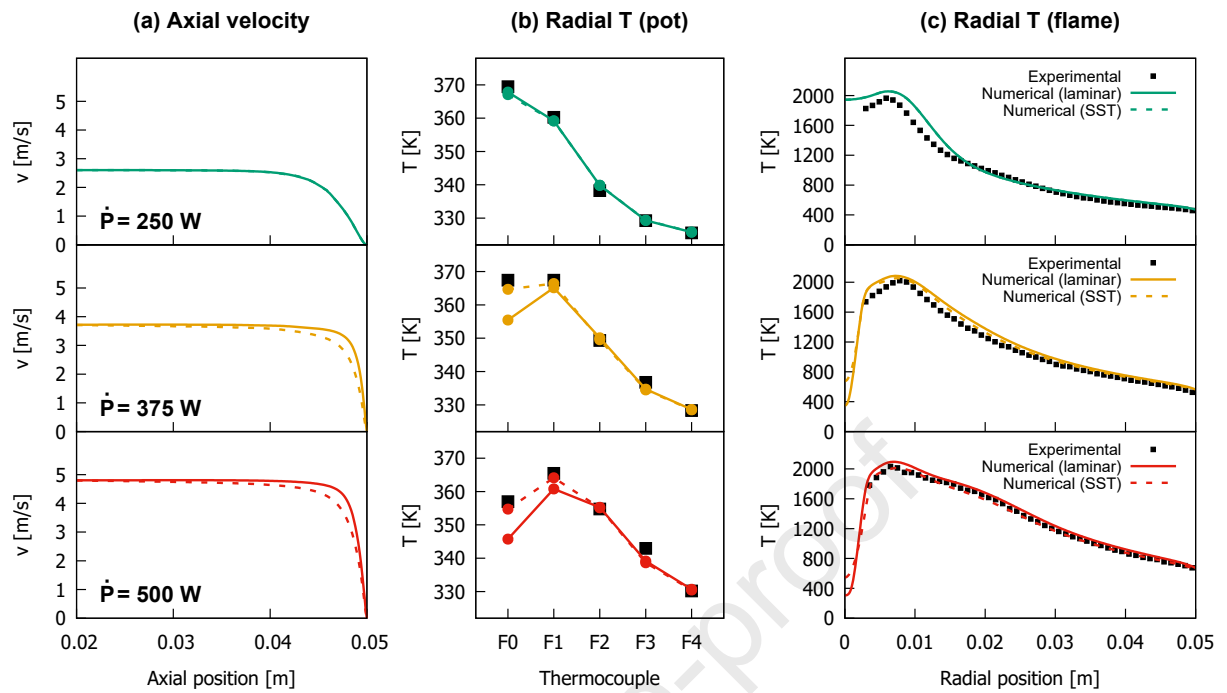


Figure 6: Characterization of the velocity magnitude along the centerline of the flame jet (a), temperature at the pot bottom wall (b), and flow field temperature near (3 mm) the pot bottom wall (c).

4.3. Temperature characterization

An accurate numerical description of temperature values is essential to obtain reliable CO emission data. Once the reacting cases are experimentally and computationally carried out, pot wall temperatures on the flame side (F0-F4) are compared in Figure 7, for different thermal power and burner-to-pot distance, with constant $\lambda=0.5$ and $T_{water}=323$ K. It can be seen that F-side temperature values are properly captured in all the cases, with a maximum deviation of ± 5 K.

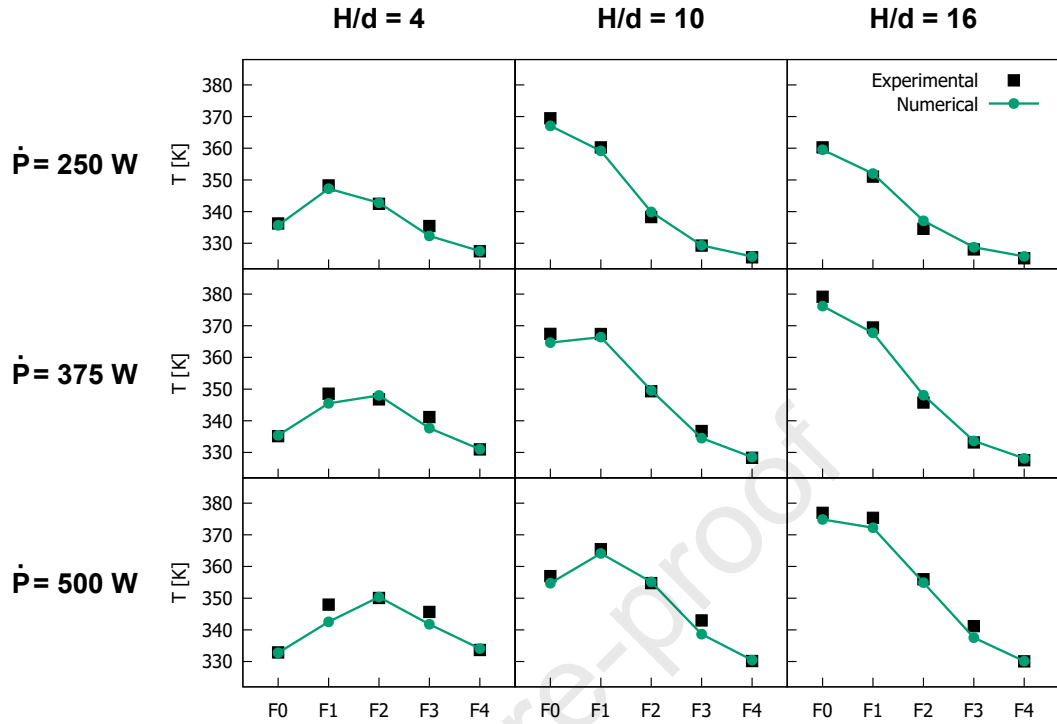


Figure 7: Measured and predicted temperature profiles on the F-side of the pot wall for different thermal power and burner-to-pot distance, at $\lambda=0.5$ and $T_{water}=323$ K.

To further evaluate the agreement between predictions and measurements, flame temperatures are analyzed and compared in Figure 8. Experimental and computational (with detailed chemistry) temperature fields are presented for the constant baseline case conditions ($H/d=10$, $\lambda=0.5$, $T_{water}=323$ K) and the three different \dot{P} cases. A significant deviation was observed in the inner core, inside the conical premixed flame. In this zone, no reaction or heat release occurs and, hence, the gas should be at low temperature, as shown in the computational contours. However, higher temperatures (1000-1500 K) were experimentally measured in that zone. This was due to an experimental artifact: the heat conduction along the thermocouple wires together with the catalytic properties of platinum induce oxidation reactions around the wires, causing significant overheating of the wires and, hence, overestimating the actual gas temperature inside the premixed flame cone. Therefore, experimental values are not a valid reference in this zone, so they are omitted from the comparison. This circumstance does not occur in the diffusion flame, where the only significant error source is due to radiative heat transfer and, as it has been indicated above, is estimated to be around 10 K.

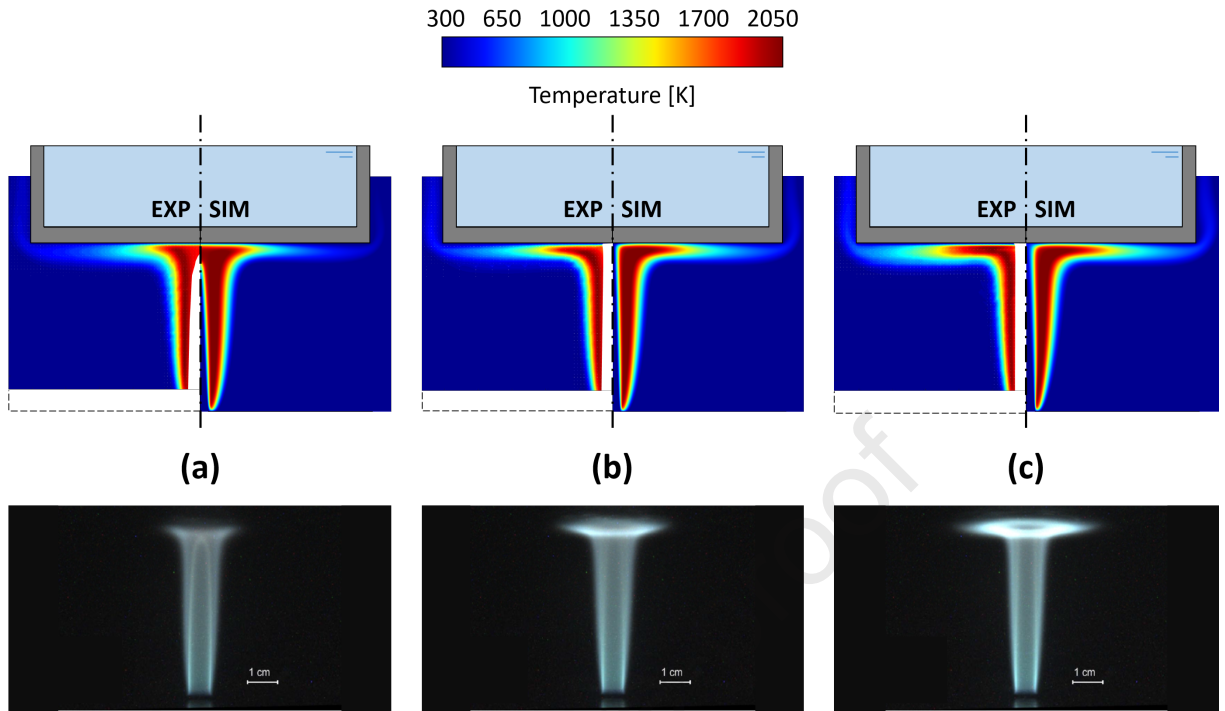


Figure 8: Experimental and numerical temperature fields comparison for (a) $\dot{P}=250$ W, (b) $\dot{P}=375$ W, and (c) $\dot{P}=500$ W (constant $H/d=10$, $\lambda=0.5$, $T_{water}=323$ K). Associated direct imaging of the flames, recorded with the video camera (visible range), are presented below.

Apart from this experimental issue, it can be generally seen a good agreement between measurements and computational temperature fields. The initial part is practically the same in the three cases, indicating that this zone is not affected by the thermal power. Once the flame reaches the pot, the remaining amount of fuel reacts in the form of a wall flame, which becomes larger as \dot{P} is raised. This increment gradually displaces the high temperatures away from the pot center, as it can be observed in the $H/d=4$ and $H/d=10$ cases of Figure 7. The agreement between experimental and numerical temperature fields is reinforced by the radial profiles comparison shown in Figure 6c.

Another important fact is related to the inner premixed flame cone. For the $\dot{P}=250$ W case, it is perfectly defined, ending at some distance from the pot wall, as it can be seen in the computational contour and the flame image of Figure 8a. For higher \dot{P} , the injection velocity increases and so does the height of the conical flame. As a result, the cold core reaches the pot wall so that the premixed flame does not exhibit a vertex but the core impinges and spreads on the cold surface for $\dot{P}=375$ and 500 W. This effect is clearly visible both in the calculated temperature maps and in the flame photographs, and explains the lower temperature registered at the F0 with respect to the F1 thermocouple in the tests with higher thermal power and/or shorter burner-to-pot distance, as shown in Figure 7. Finally, flame temperatures close to the wall are reduced due to the significant quenching effect produced by the cold wall, which may affect the final oxidation steps of certain chemical species.

4.4. Carbon monoxide characterization

Regarding emissions, CO, CO₂ and O₂ concentrations (dry basis) are measured in the exhaust gases stream. Then, CO is air-free corrected (0% oxygen). This value, frequently known as CO Air Free (COAF), is the parameter used to assess carbon monoxide emissions according to the European Standard certification [2] for domestic gas cooking burners. It can be calculated by

$$COAF = (CO)_M * \frac{(CO_2)_N}{(CO_2)_M}, \quad (3)$$

where $(CO)_M$ and $(CO_2)_M$ are respectively the volumetric percentages of CO and CO₂ collected at the hood outlet and measured on a dry basis (after removing the water vapor from the exhaust gases stream), and $(CO_2)_N$ is the volumetric percentage of CO₂ for the dry, air-free products of the neutral stoichiometric combustion of the fuel (11.7% for methane). For reference, the threshold COAF value for domestic gas cooking burners is in the range 1000-1500 ppm, depending on the type of test.

4.4.1. Effect of inside-pot water temperature

The temperature of the water inside the pot is modified by decreasing and increasing 15 K from the reference value of 323 K (constant $\dot{P}=375$ W, $H/d=10$, $\lambda=0.5$), in order to evaluate the effect of the wall temperature on CO emissions. As shown in Figure 9a, the increment in the inside-pot water temperature produces an analogous displacement in the radial temperature profile of the pot wall (flame side).

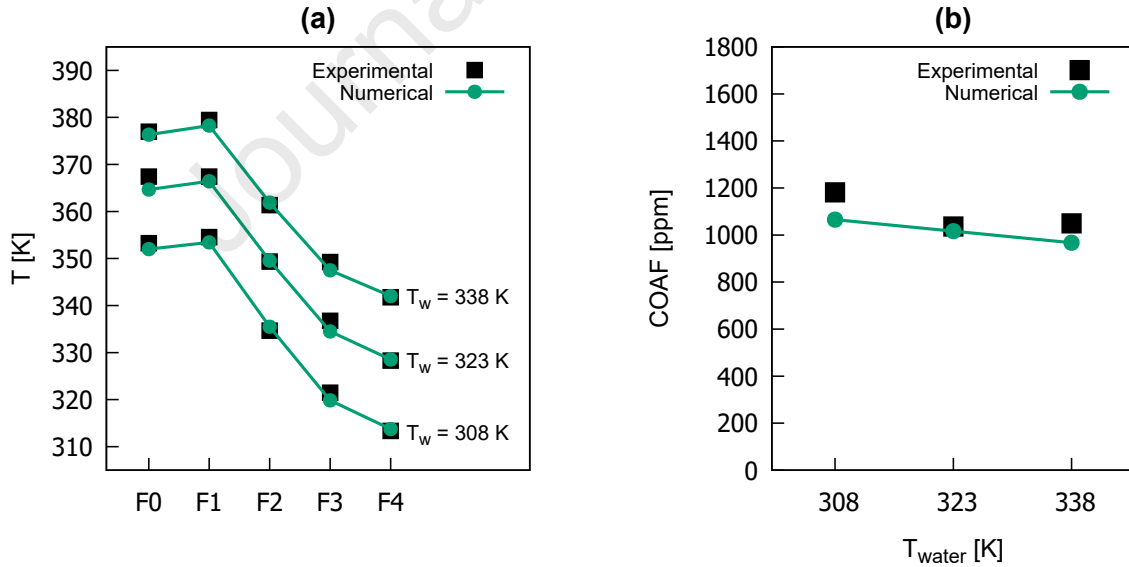


Figure 9: Temperature profiles on the F-side of the pot wall (a) and COAF evolution (b) for different inside-pot water temperatures (constant $\dot{P}=375$ W, $H/d=10$, $\lambda=0.5$).

Figure 9b shows that COAF steadily decreases as the wall becomes hotter, which seems consistent with a slight reduction of the quenching effect produced by the wall. A good agreement between measurements and numerical CO values can be observed.

4.4.2. Effect of primary aeration

Primary aeration is modified in the $\dot{P}=250$ and 375 W cases, with two additional tests about the baseline value ($\lambda=0.35, 0.5$ and 0.65), and keeping constant $H/d=10$ and $T_{water}=323$ K. As seen in Figure 10, COAF decreases for both \dot{P} as more primary air is supplied. This is an expected behavior and consistent with the higher availability of primary oxygen in the partially premixed stream, enhancing the oxidation of CO to CO₂. The agreement of measurements with GRI-Mech 3.0 is good, although, for the lowest $\lambda=0.35$, the numerical approach shows a noticeable COAF underprediction; this could be related to a mismatching in the capture of the flow pattern between the secondary air and the flame front, which leads to different physical conditions for relevant combustion reactions.

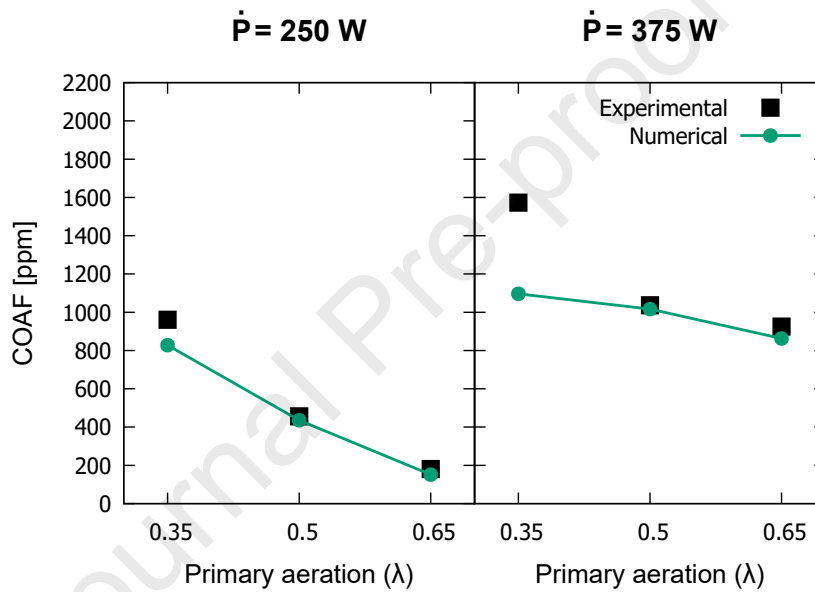


Figure 10: Effect of primary aeration (λ) in COAF values for $\dot{P}=250$ and 375 W (constant $H/d=10$, $T_{water}=323$ K).

4.4.3. Effect of flame thermal power and burner-to-pot distance

Evolution in COAF values may be analyzed either by fixing a burner-to-pot distance H/d , as directly shown in Figure 11, or by comparing points with the same thermal power \dot{P} . In all the cases, the rest of the reference conditions are kept constant ($\lambda=0.5$ and $T_{water}=323$ K). For the $H/d=16$ cases, COAF grows sharply with increasing \dot{P} . This could be seen as the usual trend [33, 37] and a consequence of a larger fraction of the reactions taking place in a wall flame (see Figure 8), with significant quenching effects in the layers closer to the wall. For the shortest burner-to-pot distance ($H/d=4$), the opposite trend is observed; this might be due to an enhanced cooling of the flame as \dot{P} is decreased, resulting in higher residual CO concentrations. At the intermediate distance ($H/d=10$), the COAF displays a maximum for $\dot{P}=375$ W, which indicates different dominant effects at each side.

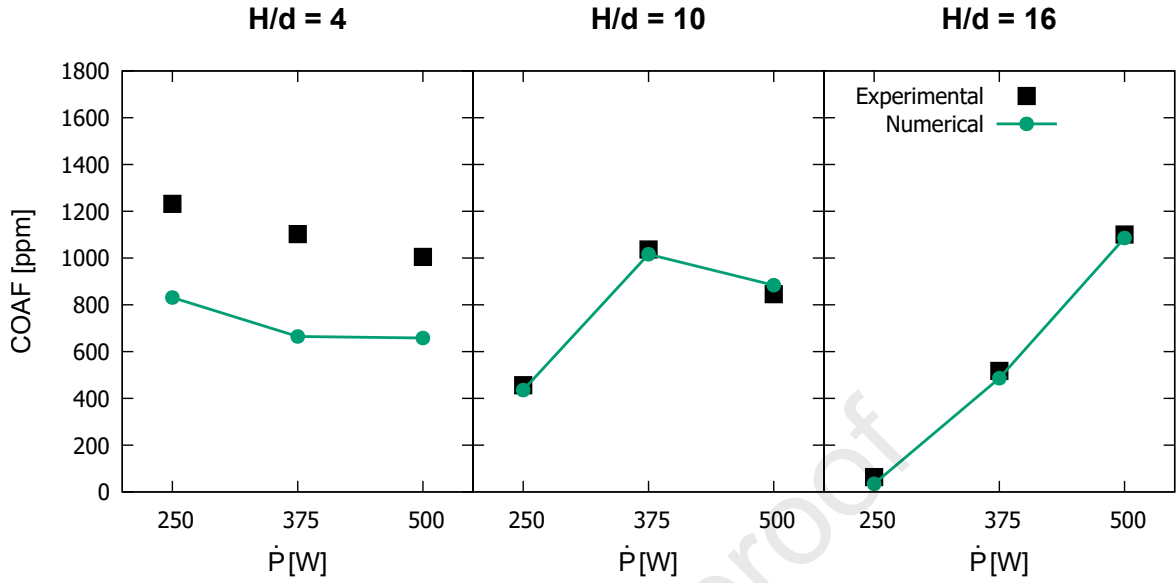


Figure 11: Effect of thermal power on COAF values at different burner-to-pot distance (constant $\lambda=0.5$, $T_{water}=323$ K).

If results are analyzed for fixed \dot{P} and variable H/d , similar trends can be observed. For $\dot{P}=250$ W, CO emissions decay as the wall is progressively located away from the injector. The significant quenching effect of the cold wall on the oxidation reactions for $H/d=4$ produces the highest CO emission; on the other hand, the flame barely impacts on the pot for $H/d=16$, which suggests that most of the carbon compounds have already been oxidized to CO_2 , leaving sparse residual CO. Different trends are observed for the medium and the high thermal power. As the pot is moved away from the burner, a peak in the numerical COAF at $H/d=10$ can be observed for fixed $\dot{P}=375$ W, while a steady rise is noticed at $\dot{P}=500$ W. This latter increment in COAF values together with the one observed when changing H/d from 4 to 10 at $\dot{P}=375$ W are due to the enhancing of the reactions of hydrocarbon radicals towards CO rather than the oxidation ones from CO to CO_2 .

Regarding the comparison between measurements and calculations, a good agreement in COAF prediction can be seen in the $H/d=10$ and $H/d=16$ cases; nevertheless, a constant deviation is observed in the $H/d=4$ ones. This discrepancy, together with the one observed for the lowest λ configuration at $\dot{P}=375$ W (Figure 10), is attributable to the combination of two factors. Firstly, the ratio between the length of the flame and the burner-to-pot distance in these cases is high enough to produce flow fluctuations that can increase the uncertainties of the experimental measurements. Secondly, these ratio may affect the numerical description of the mixing rates given by the interactions between the hot gases from the flame front and the co-flow air stream.

4.5. Flame-wall interaction analysis

In order to deeply investigate the observed COAF trends, additional simulations are carried out with the $H/d=10$ configuration and extra values of \dot{P} in the range 150-600 W, obtaining a more detailed

COAF evolution line. In these cases, a convection boundary condition is specified at the pot water-side bottom wall, with a heat transfer coefficient of $800 \text{ W/m}^2\text{K}$ and a free-stream temperature of 323 K . The rest of the boundary conditions are as previously specified. The results in Figure 12 show a maximum COAF value for $\dot{P}=375 \text{ W}$. The evolution of the thermal efficiency of the burner is also included, which is directly calculated as a ratio between the surface integral of the heat flux across the pot walls and the flame thermal power (computed from the gross calorific value of the fuel). It can be seen that this parameter follows the same trend as the COAF. Thus, for this type of configurations, there is a coincident operating point where maximum thermal efficiency always gives the maximum CO emissions, which can point out reachable design guidelines in both performance and emission thresholds.

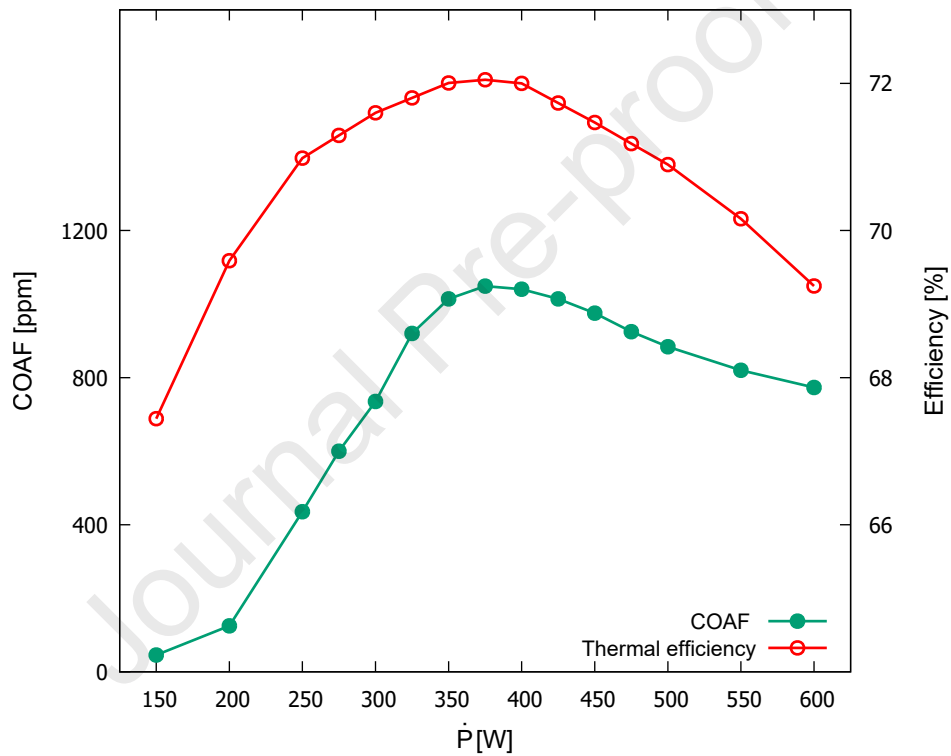


Figure 12: Detailed COAF and thermal efficiency evolution at different \dot{P} (constant $H/d=10$, $\lambda=0.5$, $T_{water}=323 \text{ K}$).

This behavior is related with the flame structure resulting from the flame interaction with the pot. The temperature contours for each case are displayed in Figure 13. It can be seen that the highest temperatures of the flame are gradually displaced from the central axis by the lower temperature of the inner premixed cone as \dot{P} increases. This cone reaches the bottom wall of the pot in the range of 350-400 W, in line with the maximum values of COAF and thermal efficiency observed in Figure 12.

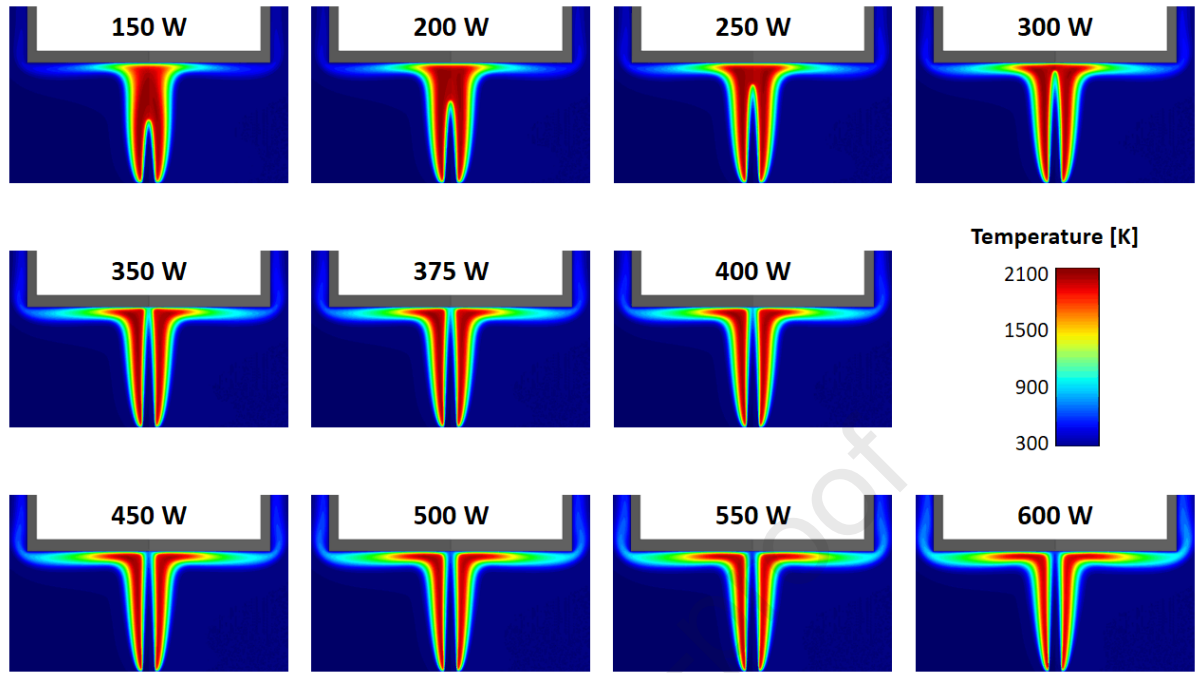


Figure 13: Computational temperature contours at different \dot{P} (constant $H/d=10$, $\lambda=0.5$, $T_{water}=323$ K).

The limit of this conical premixed flame matches with the spatial starting of the combustion reaction; kinetic studies show that the radical CH_3 is the first chemical species generated when CH_4 ignites [52, 53], so it is suitable to accurately define the premixed cone. Thus, a threshold criterion is established in this study as 10% of the maximum CH_3 concentration, represented by the iso-lines drawn in Figure 14.

The results visually confirm a direct relationship between the evolution of the inner premixed flame cone and both the CO emissions and the thermal efficiency of the burner. As \dot{P} increases, COAF and efficiency rise as long as the premixed cone is not affected by the wall. Once the flame is long enough and the rupture of the cone is produced due to its impingement with the pot, COAF and efficiency values reach their maximum, with a subsequent smoother decrease if \dot{P} keeps being raised.

This also explains the effect of flame thermal power at other burner-to-pot distances shown in Figure 11. For $H/d=4$ cases, COAF decreases because the premixed cone is broken in the three cases. On the other hand, COAF increases with \dot{P} for the $H/d=16$ cases: the pot is far enough and the breakage of the cone does not occur in none of the three cases. In general, this situation would be always observed in similar situations as long as the pot approaches and perturbs the flame.

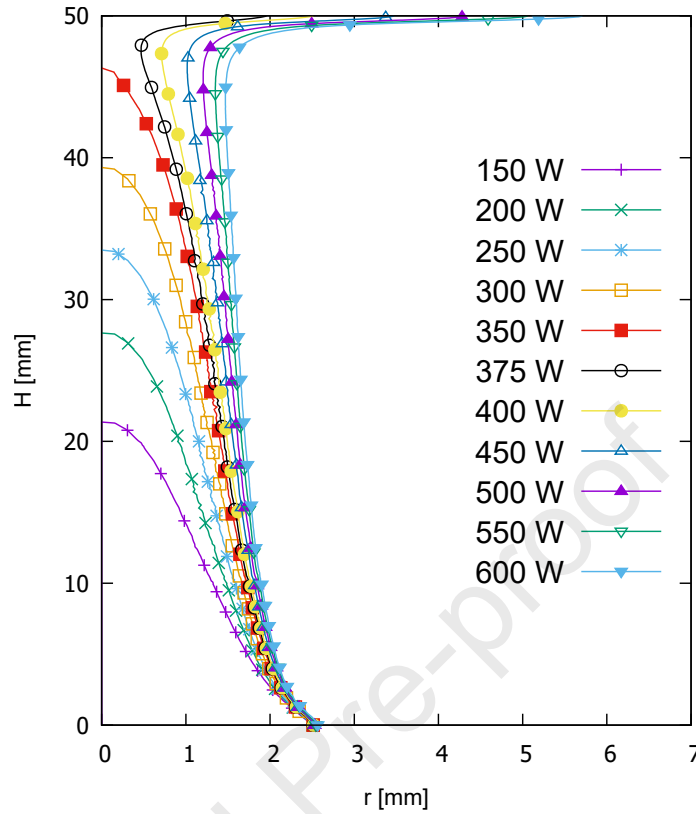


Figure 14: Limit of the conical premixed flame, represented by CH_3 concentration, at different \dot{P} (constant $H/d=10$, $\lambda=0.5$, $T_{water}=323$ K).

The global effect from the flame-wall interaction on the chemical reactions can be assessed by the definition of two parameters to evaluate the reaction completeness of the combustion. On the one hand, the oxidizer mass balance gives the amount of O_2 consumed in each configuration. Although λ is kept constant in these cases, the total mass quantity injected in the partially premixed stream depends on the \dot{P} . For this reason, the consumption value needs to be normalized by the CH_4 inlet mass flow. By stoichiometry, an ideal value of 4 kg of O_2 consumed per each kg of CH_4 supplied would represent the complete combustion. Then, the reaction completeness is lower as this consumption value moves away from 4 kg O_2 / kg CH_4 . On the other hand, the ratio between the integration of the heat released from the whole flame and the supplied heat power input can be used as another definition of the reaction completeness.

It can be observed in Figure 15 that both definitions show an alike behavior, with reverse trends to the COAF one observed in Figure 12. This fact confirms that chemical reactions are naturally affected by the evolution of the flame structure as \dot{P} changes, increasing the effects of the flame-wall interactions. Once the inner premixed flame cone reaches the pot wall, its breakage leads to a progressively lower quenching effect, radially spreading the primary mixture towards the pot lateral wall and enhancing the progress of the combustion reaction.

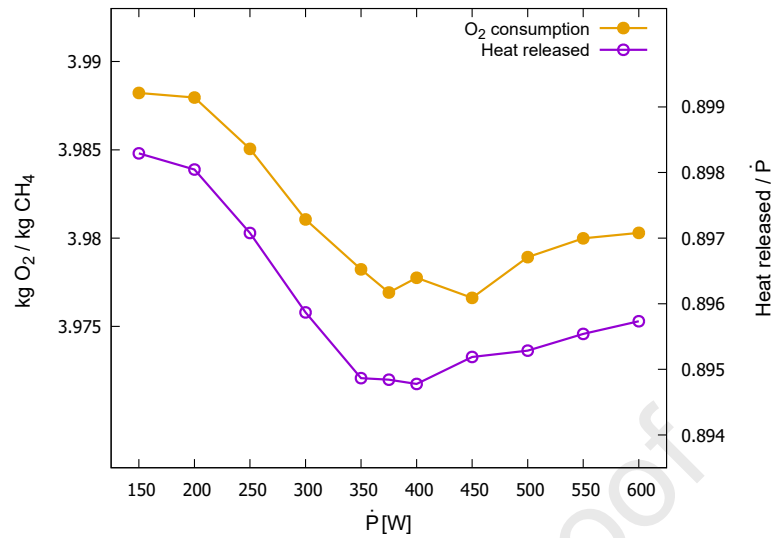


Figure 15: Assessment of the combustion reaction completeness from the consumed O₂ and the heat released from the flames (normalized with the CH₄ inlet mass flow and the thermal power respectively).

At this point, it is straightforward to assert that the structure of the flame resulting from its interaction with the pot wall is the key to the two different behaviors observed, divided by the rupture of the inner premixed flame cone. In order to evaluate how the CO formation rates are affected by the changes in the flame structure, a spatial definition of the CO-reaction zones is established. To do so, an additional conservation equation is solved for a passive scalar to individually track the two inlet streams, evolving from a value of 1 at the partially premixed fuel inlet to 0 at the air co-flow inlet (see Figure 16a). The local combination of this transported scalar and the concentration of O₂ (Figure 16b) can be used to identify the oxidizer that comes from the fuel stream (primary O₂, Figure 16c) and the air co-flow inlet (secondary O₂, Figure 16d). For further information, the reader is referred to the Supplementary Material attached to this manuscript.

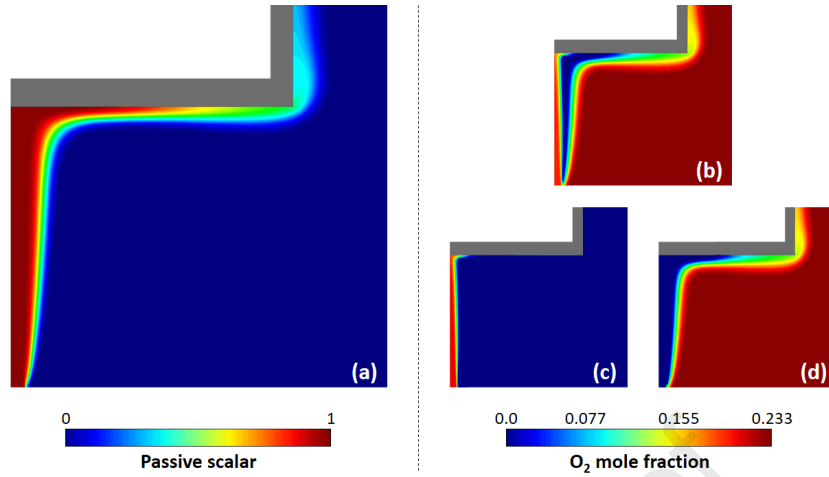


Figure 16: Distribution of the passive scalar (a) and the concentration of O₂ in the flame (b), distinguishing between the primary oxygen (c) and the secondary oxygen (d). Case conditions: $\dot{P}=375$ W, $H/d=10$, $\lambda=0.5$, $T_{water}=323$ K.

Considering only the regions of the flame where the CO chemically evolves, either by production or consumption (i.e., where the CO net reaction rate $\neq 0$), it is possible to define two different zones:

1. The CO-reacting premixed zone, as a result of the spatial combination of the regions where the CO net reaction rate $\neq 0$ and where the concentration of primary O₂ > 0 . Namely, the evolution of CO in this zone is due to the presence of oxidizer coming from the partially premixed fuel stream.
2. The CO-reacting diffusion zone, defined by the spatial coincidence of the regions where the CO net reaction rate $\neq 0$ and where the concentration of secondary O₂ > 0 . Likewise, here CO evolves due to the oxidizer that comes from the air co-flow stream.

Both zones are displayed at the top of the Figure 17 for each \dot{P} case. For the lowest \dot{P} values, the structure is similar to a free flame configuration, although naturally the hot gases need to run over the bottom and lateral pot walls by buoyancy; once the CO-reacting premixed zone reaches the pot, both regions propagate along the wall.

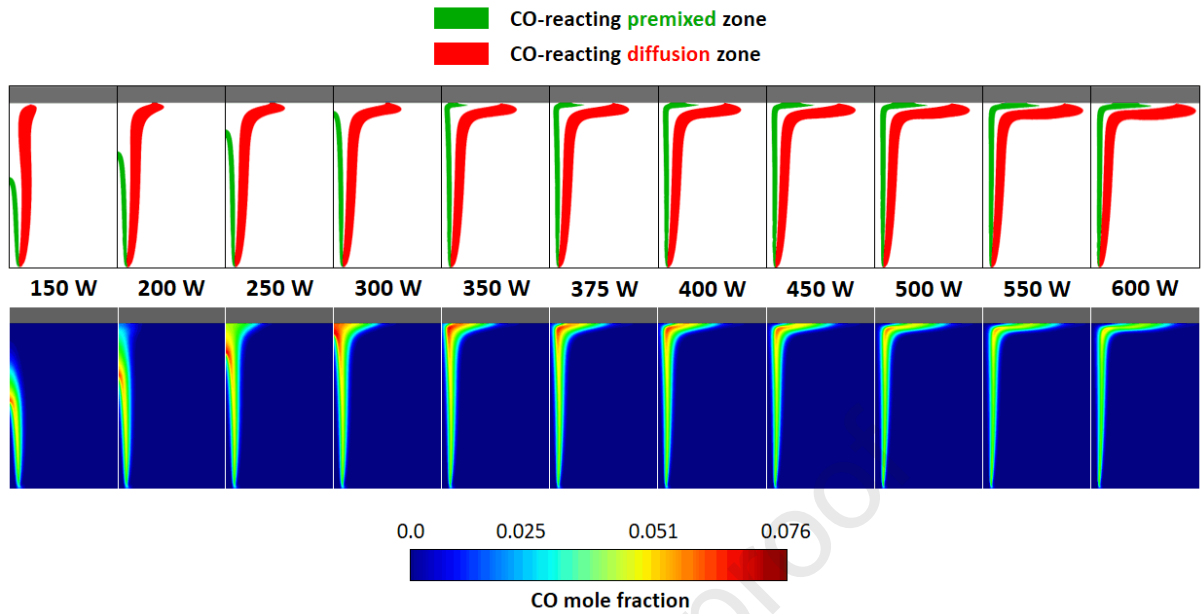


Figure 17: Evolution of the CO-reacting premixed and diffusion zones (top) and the corresponding volumetric concentration of CO (bottom) at different \dot{P} .

In the gap between the zones, the CO does not chemically react but is only transported by convection and diffusion. The highest concentrations of CO are located in this gap, as can be observed at the bottom row of Figure 17, where the corresponding CO volumetric concentration throughout the flame is shown. This means that most of the CO production occurs in the CO-reacting premixed zone, whilst its consumption predominantly takes place in the CO-reacting diffusion one. This fact is confirmed by the independent evaluation of the CO net formation inside both zones for each \dot{P} , normalized by the corresponding CH_4 inlet mass flow. As can be seen in Figure 18a, the CO-reacting premixed zone is predominantly a CO production region (net positive values), whilst the CO-reacting diffusion zone is primarily CO-consuming (net negative values). From these curves, it can be concluded that both zones are affected by the presence of the pot wall, with a stronger effect as the flame grows and approaches the pot.

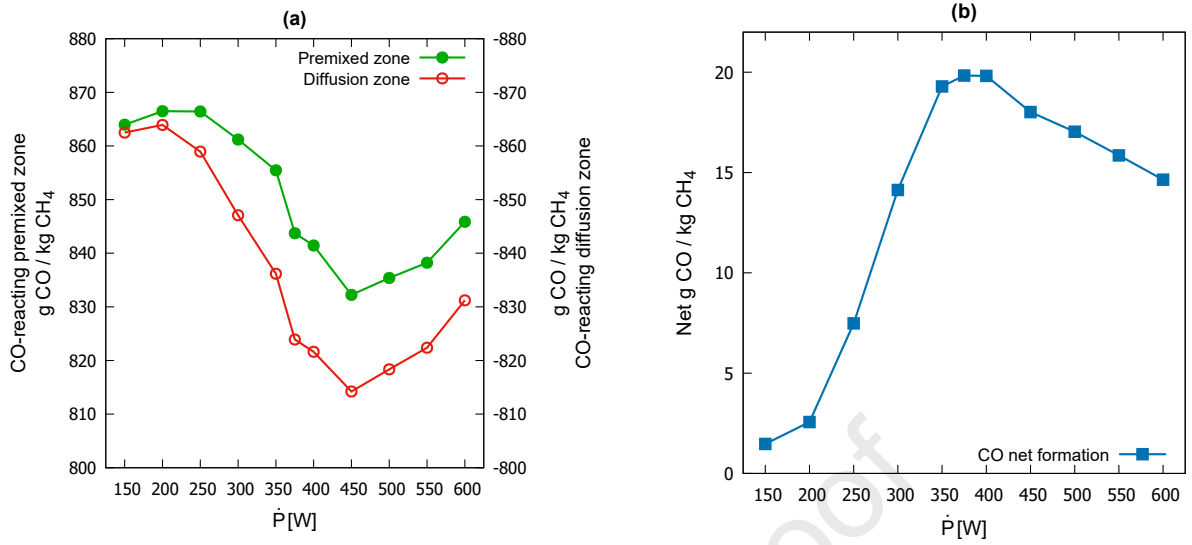


Figure 18: CO net formation at the CO-reacting premixed and diffusion zones (a) and the combination of both regions (b) at each \dot{P} .

A recovery in the growing of both the production in the premixed zone and the consumption in the diffusion zone can be observed from 450W on. The difference between every pair of values at each \dot{P} equals to the net CO formation in the flame, shown in Figure 18b. These values are naturally in agreement with the COAF results previously observed in Figure 12. The maximum CO emission value occurs near a position where the largest difference between production and consumption occurs. From this point, the CO-reacting premixed zone starts to proportionally improve its radial expansion towards the lateral pot wall (Figure 17), which corroborates that the evolution of this region is intrinsically related to the development of the net CO emissions.

To clarify the correlation between the evolution of the zones from Figure 17 and CO emissions, their two-dimensional areas are also quantified and shown in Figure 19a. A linear growing can be observed for the size of the CO-reacting diffusion zone; nevertheless, the surface growth rate of the CO-reacting premixed zone slows down from near $\dot{P}=375$ W onwards, the identified condition for the breakage of the inner premixed flame cone. Consequently, the ratio between the size of both zones (premixed over diffusion), shown in Figure 19b, tends to stabilize from that condition. This behavior agrees with the COAF trend from Figure 12. Then, the constrains for the evolution of the CO-reacting premixed zone due to the presence of the wall are responsible for the whole flame structure, modifying the local conditions (flow, temperature, species concentration) that drive the global CO net formation in the flame.

4.6. Statistical evaluation of the modeling

In order to quantify a global accuracy of the numerical approach, the weighted standard deviation is calculated, separately for temperature and COAF values, by

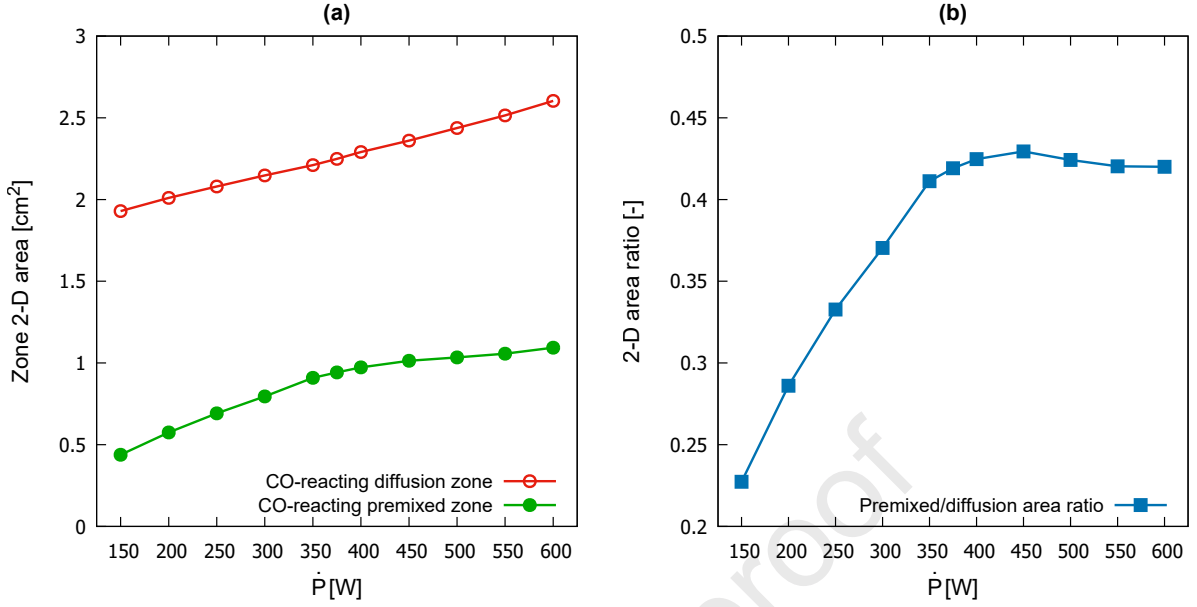


Figure 19: Two-dimensional areas of the CO-reacting premixed and diffusion zones (a) and the ratio between them (b) at each \dot{P} .

$$\sigma_w = \sqrt{\frac{1}{N-1} \sum_{i=1}^N \left(\frac{y_i - \hat{y}_i}{y_i} \right)^2}, \quad (4)$$

where y_i and \hat{y}_i are the experimental and numerical pot wall temperature (K) or COAF (ppm) values respectively, and N is the total number of the evaluated data (75 for temperature, 15 for COAF). The global error is 0.5% and 9.1% from the temperature and COAF results respectively, which is in agreement with previous findings [16].

5. Conclusions

A single, partially premixed methane flame configuration (Bunsen-like burner), impinging perpendicularly onto the bottom wall of a water pot, is designed and constructed. Temperature and CO emissions are evaluated under certain ranges of flame thermal power, burner-to-pot distance, primary aeration, and inside-pot water temperature, under similar and representative conditions of domestic gas cooking burners using natural gas. CFD simulations representing the setup are also carried out, with the detailed GRI-Mech 3.0 chemistry mechanism. The following conclusions can be drawn from this study:

- The numerical approach is able to capture all the relevant phenomena occurring in the flame: the velocity decay in the jet, the flame shape depicting the inner premixed cone and the diffusion zone, the pot wall temperature and its distribution, and the pollutants emission.
- The increase of the inside-pot water temperature produces an analogous rise on the pot wall temperature, diminishing the quenching effect that the wall produces on the flame, which implies

a reduction in CO emissions.

- If the primary aeration of the burner is raised, the higher availability of oxygen in the partially premixed stream enhances the oxidation reactions, such as those where CO evolves towards CO₂, which is translated into final lower CO emissions.
- When the burner-to-pot distance or the flame thermal power is modified, non-monotonic trends in CO emissions are observed. By means of evaluating intermediate conditions, the post-processing of the numerical results reveals a strong relationship between the internal structure of the flame and the carbon monoxide production. CO emissions rise with an increase of \dot{P} as long as the inner premixed flame cone is not affected by the wall. Once the flame is long enough and the rupture of this cone is produced due to its impingement with the pot, the CO emissions reach the maximum value, with a subsequent smoother decrease if \dot{P} keeps being raised.
- The thermal efficiency of the burner shows the same behavior as the CO emissions. Then, for this type of configurations, there is a coincident operating point where the maximum thermal efficiency is linked to the maximum CO emissions, which must be taken into account during the design process of a new NG burner.
- An extended analysis of the flame structure shows that COAF and thermal efficiency are inversely correlated to the reaction completeness of the combustion, calculated using either the O₂ consumption or the heat released from the whole flame. Besides, the distinction and study of the premixed and diffusion zones of the flame where CO chemically reacts leads to the conclusion that the final value of CO emissions is strongly driven by the flame structure resulting from its interaction with the wall. More precisely, it is mainly the propagation of the CO-reacting premixed zone which is constrained by the presence of the pot, and yields local conditions (flow, temperature, species concentration) that alter the final CO net formation.

As a general conclusion, it can be stated that CO production is slightly influenced by the temperature of the solid parts that are in contact with the flame. It is more strongly affected by the resulting structure and regions of the flame constrained by the interaction with the wall.

Some of these conclusions are of great relevance for the design of NG cooking burners. If a high value of burner thermal efficiency is sought, the conical premixed flame should be as close as possible to the pot bottom wall, by modifying either the burner thermal power or the distance from the burner ports to the pot. However, attention should be drawn to CO emissions, which will be also maximum in this operating scenario.

Acknowledgements

The authors thank Professor Norberto Fueyo and the GFN group (University of Zaragoza, Spain) for their academic support throughout the development of this work. They also thank BSH Home Appliances

for the use of its facilities and information to complete this research.

Funding

This research did not receive any specific grant from funding agencies in the public, commercial, or not-for-profit sectors.

References

- [1] D. Penney, V. Benignus, S. Kephelopoulos, D. Kotzias, M. Kleinman, A. Verrier, Carbon monoxide, in: WHO Guidelines for Indoor Air Quality: Selected Pollutants, Geneva: World Health Organization, 2010, Ch. 2, pp. 55–101, <https://www.ncbi.nlm.nih.gov/books/NBK138710>, Accessed: 2020/07/07.
- [2] European Standard, EN 30-1-1:2009-10: Domestic cooking appliances burning gas - Part 1-1: Safety - General (October 2009).
- [3] S. Chander, A. Ray, Flame impingement heat transfer: A review, *Energy Convers. Manag.* 46 (18) (2005) 2803 – 2837. doi:<https://doi.org/10.1016/j.enconman.2005.01.011>.
URL <http://www.sciencedirect.com/science/article/pii/S0196890405000324>
- [4] R. Palulli, M. Talei, R. L. Gordon, Unsteady flame–wall interaction: Impact on CO emission and wall heat flux, *Combust. Flame* 207 (2019) 406 – 416. doi:<https://doi.org/10.1016/j.combustflame.2019.06.012>.
URL <http://www.sciencedirect.com/science/article/pii/S0010218019302718>
- [5] H. Zhen, C. Leung, C. Cheung, Emission of impinging swirling and non-swirling inverse diffusion flames, *Appl. Energy* 88 (5) (2011) 1629 – 1634. doi:<https://doi.org/10.1016/j.apenergy.2010.11.036>.
URL <http://www.sciencedirect.com/science/article/pii/S030626191000499X>
- [6] U. Makmool, S. Jugjai, S. Tia, Structures and performances of laminar impinging multiple premixed LPG–air flames, *Fuel* 112 (2013) 254 – 262. doi:<https://doi.org/10.1016/j.fuel.2013.05.028>.
URL <http://www.sciencedirect.com/science/article/pii/S0016236113004407>
- [7] P. H. Barros Zárante, J. R. Sodr e, Evaluating carbon emissions reduction by use of natural gas as engine fuel, *Journal of Natural Gas Science and Engineering* 1 (6) (2009) 216 – 220. doi:<https://doi.org/10.1016/j.jngse.2009.11.002>.
URL <http://www.sciencedirect.com/science/article/pii/S1875510009000705>
- [8] H. Li, T. Wong, C. Leung, S. Probert, Thermal performances and CO emissions of gas-fired cooker-top burners, *Appl. Energy* 83 (12) (2006) 1326 – 1338. doi:<https://doi.org/10.1016/>

- j.apenergy.2006.03.002.
URL <http://www.sciencedirect.com/science/article/pii/S0306261906000389>
- [9] U. Makmool, S. Jugjai, S. Tia, Y. Laonual, P. Vallikul, B. Fungtammasan, Laser-based investigations of flow fields and OH distributions in impinging flames of domestic cooker-top burners, *Fuel* 90 (3) (2011) 1024 – 1035. doi:<https://doi.org/10.1016/j.fuel.2010.11.011>.
URL <http://www.sciencedirect.com/science/article/pii/S0016236110006113>
- [10] S.-S. Hou, C.-Y. Lee, T.-H. Lin, Efficiency and emissions of a new domestic gas burner with a swirling flame, *Energy Convers. Manag.* 48 (5) (2007) 1401 – 1410. doi:<https://doi.org/10.1016/j.enconman.2006.12.001>.
URL <http://www.sciencedirect.com/science/article/pii/S0196890406003694>
- [11] Y. Zhang, C. Qin, H. Xing, P. Liu, Experimental research on performance response of domestic gas cookers to variable natural gas constituents, *J. Nat. Gas Sci. Eng.* 10 (2013) 41 – 50. doi:<https://doi.org/10.1016/j.jngse.2012.10.004>.
URL <http://www.sciencedirect.com/science/article/pii/S187551001200114X>
- [12] Y. Zhang, W. Gao, Y. Yu, M. Wang, C. Chen, Primary air ratio change and gas interchangeability index correct for domestic gas cooker burning multi-source natural gases, *J. Nat. Gas Sci. Eng.* 35 (2016) 276 – 282. doi:<https://doi.org/10.1016/j.jngse.2016.08.060>.
URL <http://www.sciencedirect.com/science/article/pii/S1875510016306072>
- [13] C. Lacour, D. Honoré, A. Boukhalfa, R. Hauguel, Stabilization Mechanisms of Laminar Partially Premixed Flames from Domestic-Like Burner, *Combust. Sci. Technol.* 180 (1) (2007) 156–175. arXiv: <https://doi.org/10.1080/00102200701600895>, doi:10.1080/00102200701600895.
URL <https://doi.org/10.1080/00102200701600895>
- [14] Z. Chen, C. Qin, Y. Zhang, Flame stability of partially premixed combustion for PNG/LNG interchangeability, *J. Nat. Gas Sci. Eng.* 21 (2014) 467 – 473. doi:<https://doi.org/10.1016/j.jngse.2014.09.018>.
URL <http://www.sciencedirect.com/science/article/pii/S1875510014002789>
- [15] P. Boggavarapu, B. Ray, R. Ravikrishna, Thermal Efficiency of LPG and PNG-fired burners: Experimental and numerical studies, *Fuel* 116 (2014) 709 – 715. doi:<https://doi.org/10.1016/j.fuel.2013.08.054>.
URL <http://www.sciencedirect.com/science/article/pii/S0016236113007825>
- [16] S. Laguillo, J. S. Ochoa, A. Ortiz, Chemical Reaction Mechanisms Assessment for Simulation of Methane Combustion in Domestic Gas Cooking Burners, *Energy Fuels* 33 (9) (2019) 9171–9183. arXiv:<https://doi.org/10.1021/acs.energyfuels.9b01598>, doi:10.1021/acs.energyfuels.

9b01598.

URL <https://doi.org/10.1021/acs.energyfuels.9b01598>

- [17] N. Peters, Partially premixed turbulent combustion, Cambridge Monographs on Mechanics, Cambridge University Press, 2000, pp. 237–262. doi:10.1017/CB09780511612701.005.
- [18] S. Chander, A. Ray, Influence of Burner Geometry on Heat Transfer Characteristics of Methane/Air Flame Impinging on Flat Surface, *Exp. Heat Transf.* 19 (1) (2006) 15 – 38. arXiv:<https://doi.org/10.1080/08916150500317655>, doi:10.1080/08916150500317655.
URL <https://doi.org/10.1080/08916150500317655>
- [19] V. Hindasageri, R. P. Vedula, S. V. Prabhu, Heat transfer distribution for impinging methane–air premixed flame jets, *Appl. Therm. Eng.* 73 (1) (2014) 461 – 473. doi:<https://doi.org/10.1016/j.applthermaleng.2014.08.002>.
URL <http://www.sciencedirect.com/science/article/pii/S1359431114006644>
- [20] Investigation of Effect of Burner Diameter on Heat Transfer Characteristics of Methane/Air Flame Impinging on a Flat Surface, Vol. Heat Transfer: Volume 1 of ASME 2005 Summer Heat Transfer Conference collocated with the ASME 2005 Pacific Rim Technical Conference and Exhibition on Integration and Packaging of MEMS, NEMS, and Electronic Systems. arXiv:https://asmedigitalcollection.asme.org/HT/proceedings-pdf/HT2005/47314/213/2639604/213_1.pdf, doi:10.1115/HT2005-72545.
URL <https://doi.org/10.1115/HT2005-72545>
- [21] S. Chander, A. Ray, An experimental and numerical study of stagnation point heat transfer for methane/air laminar flame impinging on a flat surface, *Int. J. Heat Mass Transf.* 51 (13) (2008) 3595 – 3607. doi:<https://doi.org/10.1016/j.ijheatmasstransfer.2007.10.018>.
URL <http://www.sciencedirect.com/science/article/pii/S0017931007006436>
- [22] S. Chander, A. Ray, Experimental and numerical study on the occurrence of off-stagnation peak in heat flux for laminar methane/air flame impinging on a flat surface, *Int. J. Heat Mass Transf.* 54 (5) (2011) 1179 – 1186. doi:<https://doi.org/10.1016/j.ijheatmasstransfer.2010.10.035>.
URL <http://www.sciencedirect.com/science/article/pii/S0017931010006150>
- [23] M. Morad, A. Momeni, E. E. Fordoei, M. Ashjaee, Experimental and numerical study on heat transfer characteristics for methane/air flame impinging on a flat surface, *Int. J. Therm. Sci.* 110 (2016) 229 – 240. doi:<https://doi.org/10.1016/j.ijthermalsci.2016.07.005>.
URL <http://www.sciencedirect.com/science/article/pii/S1290072915304233>
- [24] S. Tuttle, B. Webb, M. McQuay, Convective heat transfer from a partially premixed impinging flame jet. Part I: Time-averaged results, *Int. J. Heat Mass Transf.* 48 (7) (2005) 1236 – 1251. doi:<https://doi.org/10.1016/j.ijheatmasstransfer.2005.06.018>.

- [//doi.org/10.1016/j.ijheatmasstransfer.2004.10.027](https://doi.org/10.1016/j.ijheatmasstransfer.2004.10.027).
URL <http://www.sciencedirect.com/science/article/pii/S0017931004004934>
- [25] S. Tuttle, B. Webb, M. McQuay, Convective heat transfer from a partially premixed impinging flame jet. Part II: Time-resolved results, *Int. J. Heat Mass Transf.* 48 (7) (2005) 1252 – 1266. doi:<https://doi.org/10.1016/j.ijheatmasstransfer.2004.10.028>.
URL <http://www.sciencedirect.com/science/article/pii/S0017931004004946>
- [26] S.-S. Hou, Y.-C. Ko, Effects of heating height on flame appearance, temperature field and efficiency of an impinging laminar jet flame used in domestic gas stoves, *Energy Convers. Manag.* 45 (9) (2004) 1583 – 1595. doi:<https://doi.org/10.1016/j.enconman.2003.09.016>.
URL <http://www.sciencedirect.com/science/article/pii/S019689040300267X>
- [27] V. C. Raj, P. Kuntikana, S. Sreedhara, S. Prabhu, Separation of heat transfer components from impinging methane diffusion flames, *Int. J. Heat Mass Transf.* 126 (2018) 123 – 138. doi:<https://doi.org/10.1016/j.ijheatmasstransfer.2018.05.014>.
URL <http://www.sciencedirect.com/science/article/pii/S001793101830156X>
- [28] V. C. Raj, P. Kuntikana, S. Sreedhara, S. Prabhu, Heat transfer characteristics of impinging methane diffusion and partially premixed flames, *Int. J. Heat Mass Transf.* 129 (2019) 873 – 893. doi:<https://doi.org/10.1016/j.ijheatmasstransfer.2018.10.009>.
URL <http://www.sciencedirect.com/science/article/pii/S0017931018324980>
- [29] W.-D. Hsieh, T.-H. Lin, Methane flame stability in a jet impinging onto a wall, *Energy Convers. Manag.* 46 (5) (2005) 727 – 739. doi:<https://doi.org/10.1016/j.enconman.2004.05.010>.
URL <http://www.sciencedirect.com/science/article/pii/S0196890404001207>
- [30] S.-S. Hou, Y.-C. Ko, Influence of oblique angle and heating height on flame structure, temperature field and efficiency of an impinging laminar jet flame, *Energy Convers. Manag.* 46 (6) (2005) 941 – 958. doi:<https://doi.org/10.1016/j.enconman.2004.06.001>.
URL <http://www.sciencedirect.com/science/article/pii/S0196890404001311>
- [31] P. Kuntikana, S. Prabhu, Heat transfer characteristics of premixed methane–air flame jet impinging obliquely onto a flat surface, *Int. J. Heat Mass Transf.* 101 (2016) 133 – 146. doi:<https://doi.org/10.1016/j.ijheatmasstransfer.2016.05.004>.
URL <http://www.sciencedirect.com/science/article/pii/S0017931016303325>
- [32] A. R. Tajik, P. Kuntikana, S. V. Prabhu, V. Hindasageri, Effect of preheated mixture on heat transfer characteristics of impinging methane–air premixed flame jet, *Int. J. Heat Mass Transf.* 86 (2015) 550 – 562. doi:<https://doi.org/10.1016/j.ijheatmasstransfer.2015.03.040>.
URL <http://www.sciencedirect.com/science/article/pii/S0017931015002987>

- [33] C. Saha, R. Ganguly, A. Datta, Heat Transfer and Emission Characteristics of Impinging Rich Methane and Ethylene Jet Flames, *Exp. Heat Transf.* 21 (3) (2008) 169 – 187. arXiv:<https://doi.org/10.1080/08916150802072834>, doi:10.1080/08916150802072834.
URL <https://doi.org/10.1080/08916150802072834>
- [34] A. Singh, M. Mann, T. Kissel, J. Brübach, A. Dreizler, Simultaneous Measurements of Temperature and CO Concentration in Stagnation Stabilized Flames, *Flow Turbul. Combust.* 90 (4) (2013) 723–739. doi:10.1007/s10494-011-9384-6.
URL <https://doi.org/10.1007/s10494-011-9384-6>
- [35] M. Mann, C. Jainski, M. Euler, B. Böhm, A. Dreizler, Transient flame-wall interactions: Experimental analysis using spectroscopic temperature and CO concentration measurements, *Combust. Flame* 161 (9) (2014) 2371 – 2386. doi:<https://doi.org/10.1016/j.combustflame.2014.02.008>.
URL <http://www.sciencedirect.com/science/article/pii/S0010218014000674>
- [36] Y.-C. Chien, D. Escofet-Martin, D. Dunn-Rankin, CO emission from an impinging non-premixed flame, *Combust. Flame* 174 (2016) 16 – 24. doi:<https://doi.org/10.1016/j.combustflame.2016.09.004>.
URL <http://www.sciencedirect.com/science/article/pii/S0010218016302486>
- [37] H. Li, H. Zhen, C. Leung, C. Cheung, Effects of plate temperature on heat transfer and emissions of impinging flames, *Int. J. Heat Mass Transf.* 53 (19) (2010) 4176 – 4184. doi:<https://doi.org/10.1016/j.ijheatmasstransfer.2010.05.040>.
URL <http://www.sciencedirect.com/science/article/pii/S0017931010002826>
- [38] H. Li, H. Zhen, C. Leung, C. Cheung, Nozzle effect on heat transfer and CO emission of impinging premixed flames, *Int. J. Heat Mass Transf.* 54 (1) (2011) 625 – 635. doi:<https://doi.org/10.1016/j.ijheatmasstransfer.2010.09.008>.
URL <http://www.sciencedirect.com/science/article/pii/S0017931010004850>
- [39] D. Mishra, Emission studies of impinging premixed flames, *Fuel* 83 (13) (2004) 1743 – 1748. doi:<https://doi.org/10.1016/j.fuel.2004.02.019>.
URL <http://www.sciencedirect.com/science/article/pii/S0016236104000687>
- [40] European Standard, DIN EN 437:2009-09, in: Test gases - Test pressures - Appliance categories (includes Amendment A1:2009), 2009, p. 46.
- [41] H. K. Kayadelen, Effect of natural gas components on its flame temperature, equilibrium combustion products and thermodynamic properties, *Journal of Natural Gas Science and Engineering* 45 (2017) 456 – 473. doi:<https://doi.org/10.1016/j.jngse.2017.05.023>.
URL <http://www.sciencedirect.com/science/article/pii/S1875510017302457>

- [42] F. E. Jørgensen, Uncertainty of CTA measurements, in: F. E. Jørgensen (Ed.), *How to measure turbulence with hot-wire anemometers - a practical guide*, Dantec Dynamics, 2002, pp. 40–44.
- [43] C. Shaddix, Correcting thermocouple measurements for radiation loss: A critical review, in: *33rd National Heat Transfer Conference NHTC'99*, Albuquerque, NM (US), 08/15 - 08/17, 1999, pp. 1–10.
- [44] M. P. Remacha, S. Jiménez, J. Ballester, Devolatilization of millimeter-sized biomass particles at high temperatures and heating rates. Part 1: Experimental methods and results, *Fuel* 234 (2018) 757 – 769. doi:<https://doi.org/10.1016/j.fuel.2018.07.016>.
URL <http://www.sciencedirect.com/science/article/pii/S001623611831216X>
- [45] ANSYS Fluent Theory and User's Guide, release 18.2; ANSYS, Inc. (2017).
- [46] F. R. Menter, R. B. Langtry, S. R. Likki, Y. B. Suzen, P. G. Huang, S. Völker, A Correlation-Based Transition Model Using Local Variables—Part I: Model Formulation, *J. Turbomach.* 128 (3) (2004) 413–422. arXiv:https://asmedigitalcollection.asme.org/turbomachinery/article-pdf/128/3/413/4877819/413_1.pdf, doi:10.1115/1.2184352.
URL <https://doi.org/10.1115/1.2184352>
- [47] F. R. Menter, R. Langtry, S. Völker, Transition Modelling for General Purpose CFD Codes, *Flow Turbul. Combust.* 77 (1) (2006) 277–303. doi:10.1007/s10494-006-9047-1.
URL <https://doi.org/10.1007/s10494-006-9047-1>
- [48] G. Smith, D. Golden, M. Frenklach, N. Moriarty, B. Eiteneer, M. Goldenberg, C. Bowman, R. Hanson, S. Song, W. Gardiner Jr., V. Lissianski, Z. Qin, GRI-Mech Version 3.0 (1999), available from: <http://combustion.berkeley.edu/gri-mech/version30/text30.html> (accessed August 19, 2019).
- [49] S. R. Mathur, J. Y. Murthy, Coupled Ordinates Method for Multigrid Acceleration of Radiation Calculations, *J. Thermophys. Heat Transf.* 13 (4) (1999) 467–473. arXiv:<https://doi.org/10.2514/2.6485>, doi:10.2514/2.6485.
URL <https://doi.org/10.2514/2.6485>
- [50] J. Hameury, B. Hay, J. R. Filtz, Measurement of Total Hemispherical Emissivity Using a Calorimetric Technique, *Int. J. Thermophys.* 28 (5) (2007) 1607 – 1620. doi:10.1007/s10765-007-0213-z.
URL <https://doi.org/10.1007/s10765-007-0213-z>
- [51] S. B. Pope, *Turbulent Flows*, Cambridge University Press, 2000. doi:10.1017/CB09780511840531.
- [52] J. Warnatz, Rate coefficients in the C=H=O system, in: Gardiner, W.C. Jr. (Ed.), *Combustion Chemistry*, Springer-Verlag, NY, 1984, pp. 197 – 360.

- [53] S. Stocker, G. Csányi, K. Reuter, J. T. Margraf, Machine learning in chemical reaction space, Nat. Commun. 11 (1). doi:10.1038/s41467-020-19267-x.

Journal Pre-proof

Highlights:

- The interaction of a single methane flame with the wall of a water pot is analyzed.
- Variable thermal power, burner-pot distance, primary aeration and wall temperature.
- Experimental tests and CFD simulations of the setup are carried out.
- CO emissions are influenced by the relative position of the conical premixed flame.
- Energy efficiency also depends on the inner premixed flame cone location.

Declaration of interests

The authors declare that they have no known competing financial interests or personal relationships that could have appeared to influence the work reported in this paper.

The authors declare the following financial interests/personal relationships which may be considered as potential competing interests:

Journal Pre-proof